Report Number: FTA-DC-26-7098-02.1

SAND2003-0733P
Printed March 2004

SERAPHIM Urban Maglev Propulsion Design

June 2002

Published by:
Sandia National Laboratories
Beam Applications and Initiatives Department
Albuquerque, NM 87185-1182

Prepared for:
Federal Transit Administration
Office of Research, Demonstration and Innovation
U.S. Department of Transportation
Washington, DC 20590

This page is intentionally left blank

REPORT DOCUMENTATION PAGE

Form Approved
OMB No. 0704-0188

1. AGENCY USE ONLY (Leave blank)	2. REPORT DATE	3. REPORT TYPE AND DATES COVERED
	2002	Project Report, 2001

4. TITLE AND SUBTITLE
SERAPHIM Urban Maglev Propulsion Design

5. FUNDING NUMBERS

6. AUTHOR(S)
R.J. Kaye, W.R. Chambers, J.F. Dempsey, R.C. Dykhuizen, J.B. Kelley, G.A. Mann, B.M. Marder, and B.N. Turman

7. PERFORMING ORGANIZATION NAME(S) AND ADDRESS(ES)
Sandia National Laboratories
P.O. Box 5800
Albuquerque, NM 87185-1182

8. PERFORMING ORGANIZATION REPORT NUMBER
SAND2003-0733P

9. SPONSORING/MONITORING AGENCY NAME(S) AND ADDRESS(ES)
U.S. Department of Transportation
Federal Transit Administration, Office of Technology,
400 7th Street, SW, Washington, DC 20590

10. SPONSORING/MONITORING AGENCY REPORT NUMBER
FTA-DC-26-7098-02.1

11. SUPPLEMENTARY NOTES

12a. DISTRIBUTION/AVAILABILITY STATEMENT
Available From: National Technical Information Service/NTIS, Springfield, Virginia, 22161. Phone 703.605.6000, Fax 703.605.6900, Email [orders@ntis.fedworld.gov]

12b. DISTRIBUTION CODE

13. ABSTRACT (Maximum 200 words)
The SERAPHIM linear induction motor consists of air-core, discretely-energized coils capable of efficiently providing high thrust at low and high speed. With the potential for a low-cost guideway by the use of a wide clearance between active vehicle coils and passive track coils, this propulsion system is being evaluated for applications in low-speed urban maglev transit. A concept four-coil motor has been developed to meet the requirements of an urban transit route that could include a mountainous section based on information from the Low-Speed Maglev Technology Development Program and the Colorado Department of Transportation I-70 Mountain Programmatic Environmental Impact Study. The concept includes definition of the track coils, power supply, and cooling systems. Thrust and efficiency curves are calculated using an improved motor-circuit-analysis code using normal and high-temperature superconductors (HTS). The design of a half-scale motor coil to operate at stress levels necessary to meet urban transit applications is presented that includes electrical, thermal, and mechanical stress analysis. Fabrication of coils and power supply is in progress for evaluation in a static test stand that also includes cooling, diagnostics, controls, and support structure. Test plans for the coil evaluation are discussed.

14. SUBJECT TERMS
linear induction motor, maglev, propulsion, urban transit

15. NUMBER OF PAGES
56

16. PRICE CODE

17. SECURITY CLASSIFICATION OF REPORT	18. SECURITY CLASSIFICATION OF THIS PAGE	19. SECURITY CLASSIFICATION OF ABSTRACT	20. LIMITATION OF ABSTRACT
Unclassified	Unclassified	Unclassified	

NSN 7540-01-280-5500 Standard Form 298 (Rev. 2-89)
Prescribed by ANSI Std. 239-18298-102

NOTICE

This document is disseminated under the sponsorship of the U.S. Department of Transportation in the interest of information exchange. The United States Government assumes no liability for its contents or use thereof.

The United States Government does not endorse products of manufacturers. Trade or manufacturers' names appear herein solely because they are considered essential to the objective of this report.

METRIC/ENGLISH CONVERSION FACTORS

ENGLISH TO METRIC

LENGTH (APPROXIMATE)

1 inch (in)	=	2.5 centimeters (cm)
1 foot (ft)	=	30 centimeters (cm)
1 yard (yd)	=	0.9 meter (m)
1 mile (mi)	=	1.6 kilometers (km)

AREA (APPROXIMATE)

1 square inch (sq in, in^2)	=	6.5 square centimeters (cm^2)
1 square foot (sq ft, ft^2)	=	0.09 square meter (m^2)
1 square yard (sq yd, yd^2)	=	0.8 square meter (m^2)
1 square mile (sq mi, mi^2)	=	2.6 square kilometers (km^2)
1 acre = 0.4 hectare (he)	=	4,000 square meters (m^2)

MASS - WEIGHT (APPROXIMATE)

1 ounce (oz)	=	28 grams (gm)
1 pound (lb)	=	0.45 kilogram (kg)
1 short ton = 2,000 pounds (lb)	=	0.9 tonne (t)

VOLUME (APPROXIMATE)

1 teaspoon (tsp)	=	5 milliliters (ml)
1 tablespoon (tbsp)	=	15 milliliters (ml)
1 fluid ounce (fl oz)	=	30 milliliters (ml)
1 cup (c)	=	0.24 liter (l)
1 pint (pt)	=	0.47 liter (l)
1 quart (qt)	=	0.96 liter (l)
1 gallon (gal)	=	3.8 liters (l)
1 cubic foot (cu ft, ft^3)	=	0.03 cubic meter (m^3)
1 cubic yard (cu yd, yd^3)	=	0.76 cubic meter (m^3)

TEMPERATURE (EXACT)

[(x-32)(5/9)] °F = y °C

METRIC TO ENGLISH

LENGTH (APPROXIMATE)

1 millimeter (mm)	=	0.04 inch (in)
1 centimeter (cm)	=	0.4 inch (in)
1 meter (m)	=	3.3 feet (ft)
1 meter (m)	=	1.1 yards (yd)
1 kilometer (km)	=	0.6 mile (mi)

AREA (APPROXIMATE)

1 square centimeter (cm^2)	=	0.16 square inch (sq in, in^2)
1 square meter (m^2)	=	1.2 square yards (sq yd, yd^2)
1 square kilometer (km^2)	=	0.4 square mile (sq mi, mi^2)
10,000 square meters (m^2)	=	1 hectare (ha) = 2.5 acres

MASS - WEIGHT (APPROXIMATE)

1 gram (gm)	=	0.036 ounce (oz)
1 kilogram (kg)	=	2.2 pounds (lb)
1 tonne (t)	=	1,000 kilograms (kg)
	=	1.1 short tons

VOLUME (APPROXIMATE)

1 milliliter (ml)	=	0.03 fluid ounce (fl oz)
1 liter (l)	=	2.1 pints (pt)
1 liter (l)	=	1.06 quarts (qt)
1 liter (l)	=	0.26 gallon (gal)
1 cubic meter (m^3)	=	36 cubic feet (cu ft, ft^3)
1 cubic meter (m^3)	=	1.3 cubic yards (cu yd, yd^3)

TEMPERATURE (EXACT)

[(9/5) y + 32] °C = x °F

QUICK INCH - CENTIMETER LENGTH CONVERSION

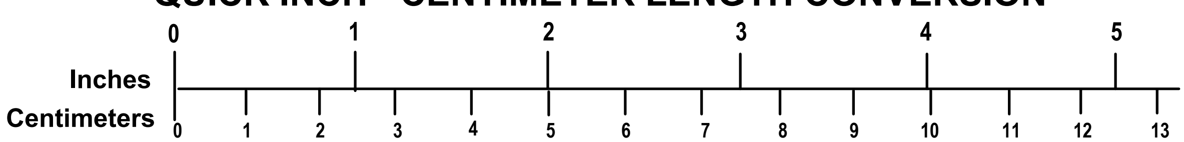

QUICK FAHRENHEIT - CELSIUS TEMPERATURE CONVERSION

°F	-40°	-22°	-4°	14°	32°	50°	68°	86°	104°	122°	140°	158°	176°	194°	212°
°C	-40°	-30°	-20°	-10°	0°	10°	20°	30°	40°	50°	60°	70°	80°	90°	100°

For more exact and or other conversion factors, see NIST Miscellaneous Publication 286, Units of Weights and Measures. Price $2.50 SD Catalog No. C13 10286

Updated 6/17/98

This page is intentionally left blank

SERAPHIM Urban Maglev Propulsion Design

FTA Project DC-26-7098

June 7, 2002

R.J. Kaye, W.R. Chambers, J.F. Dempsey, R.C. Dykhuizen, J.B. Kelley, G.A. Mann,
B.M. Marder, and B.N. Turman
Sandia National Laboratories, Albuquerque, New Mexico, 87185-1182[i]

Abstract

The SERAPHIM linear induction motor consists of air-core, discretely-energized coils capable of efficiently providing high thrust at low and high speed. With the potential for a low-cost guideway by the use of a wide clearance between active vehicle coils and passive track coils, this propulsion system is being evaluated for applications in low-speed urban maglev transit. A concept four-coil motor has been developed to meet the requirements of an urban transit route that could include a mountainous section based on information from the Low-Speed Maglev Technology Development Program and the Colorado Department of Transportation I-70 Mountain Programmatic Environmental Impact Study. The concept includes definition of the track coils, power supply, and cooling systems. Thrust and efficiency curves are calculated using an improved motor-circuit-analysis code using normal and high-temperature superconductors (HTS). The design of a half-scale motor coil to operate at stress levels necessary to meet urban transit applications is presented that includes electrical, thermal, and mechanical stress analysis. Fabrication of coils and power supply is in progress for evaluation in a static test stand that also includes cooling, diagnostics, controls, and support structure. Test plans for the coil evaluation are discussed.

[i] Sandia is a multiprogram laboratory operated by Sandia Corporation, a Lockheed Martin Company, for the United States Department of Energy's National Nuclear Security Administration under contract DE-AC04-94-AL85000.

This page is intentionally left blank

TABLE OF CONTENTS

TABLE OF CONTENTS **3**

LIST OF FIGURES **4**

LIST OF TABLES **7**

ACKNOWLEDGEMENT **8**

INTRODUCTION **9**

- PREVIOUS STUDIES 9
- APPLICATION TO LOW-SPEED URBAN MAGLEV 10

DESIGN BASIS **12**

MOTOR CONCEPT AND PERFORMANCE CALCULATIONS **15**

SUPERCONDUCTOR OPTION FOR THE SERAPHIM MOTOR **19**

- THE PROMISE OF SUPERCONDUCTIVITY 19
- THE PROBLEMS OF SUPERCONDUCTIVITY 19
- ANALYSIS OF EFFECT OF HTS ON SYSTEM EFFICIENCY 19
- ANALYSIS OF EFFECT OF HTS ON SYSTEM PERFORMANCE 20
- ANALYSIS OF MOTOR COIL PERFORMANCE WITH SUPERCONDUCTING WINDING 22
  - *Baseline case: Normal conductor* *22*
  - *Superconductor cases* *24*
- SUMMARY AND CONCLUSIONS ON SUPERCONDUCTIVITY 26

COIL DESIGN **27**

- MEASUREMENT OF COIL LOSSES 28
- MITIGATION OF INCREASED AC RESISTANCE 29
- THERMAL DESIGN OF SERAPHIM MOTOR 31
  - *Track coil cooling requirements* *31*
  - *Motor Coil Coolant Channel Geometry* *32*
  - *Cooling Fluid* *34*
  - *Fluid Distribution* *34*
  - *Axial Channel Pressure Drop and Heat Transfer* *35*
  - *Coolant Flow: Plenum Geometry* *36*
  - *Coolant Flow: Circumferential header geometry* *39*
  - *Conclusions from Thermal Design* *40*
- MODELING AND STRESS ANALYSIS OF SERAPHIM STATIC TESTBED COILS 41
  - *SERAPHIM motor coil design options* *41*
  - *SERAPHIM testbed coil modeling* *41*
  - *Results* *43*

PLANNED TESTING **49**

FUTURE DEVELOPMENT **51**

SUMMARY **52**

REFERENCES **54**

LIST OF FIGURES

Figure 1. Basic SERAPHIM motor configuration using one motor coil and multiple track coils. ... 9

Figure 2. Each vehicle powered by 4-coil SERAPHIM motor. Red coils are powered at position shown. Green coils, presently unpowered, will be energized as vehicle moves them into optimum position for thrust. ... 9

Figure 3. Potential route for maglev transit system in Denver metropolitan area. Test case route used to determine basis for coil design is along I-70 from Colorado 470 to the Hidden Valley exit. ... 12

Figure 4. Typical thrust versus speed curve developed for SERAPHIM motor to achieve high thrust at low speed, then decreasing inversely with speed above a critical speed that sets a maximum mechanical power. ... 13

Figure 5. Elevation profile and speed limit for route segment used to determine motor thrust and power requirements. ... 14

Figure 6. Block diagram of circuit driving a four-coil SERAPHIM motor, where the on-board motor coils are switched sequentially to the inverter-capacitor power supply to provide optimum thrust or braking. ... 15

Figure 7. One of several motor coil and track circuits analyzed by the SERTRAIN code. The transient, coil current response is calculated based on the variable frequency voltage forcing function from the inverter applied to the resonant capacitor-coil(s). ... 16

Figure 8. Polarity of applied voltage from inverter is synchronized with voltage across the capacitor so the capacitor maintains the same peak value in each oscillation cycle, and provides the same power when switched to another motor coil. ... 17

Figure 9. Instantaneous and time-averaged thrust and lift forces from interaction of a single motor and track coil. Although the coil has a radius of 0.4 m, the power is switched to a different coil at 0.33 m at the time of zero current in the motor coil. ... 18

Figure 10. Average efficiency of full-scale motor at power pickup calculated with SERTRAIN circuit code, including an estimated 90% efficiency for the rectifier/inverter. ... 18

Figure 11. Comparison of lossless HTS to normal motor efficiency ignoring electrical requirement of cryo-cooling system. The calculation assumes the power supply efficiency is 90%. 21

Figure 12. Geometry of baseline normal-conducting winding motor and track coil. ... 22

Figure 13. Diagram of circuit modeled for normal conductor baseline case. ... 23

Figure 14. Current histories for motor (Ic) and track coils and inverter output current (Isource) feeding resonant capacitor. Position shown on abscissa is displacement between centers of motor and track coil. ... 24

Figure 15. Possible positions, A, B, or C, of superconducting motor coil winding within housing. ... 25

Figure 16. Cutaway of sub-scale coil designed for the static testbed. ... 28

Figure 17. Test coil in dielectric housing to measure winding resistance increase due to eddy currents. Outer diameter of housing is 45.7 cm. ... 28

Figure 18. Resistance measurement of test coil as a function of the ratio of wire thickness to skin depth. Wire conductor size is 0.58 cm. Calculated DC resistance of coil is 45.8 mΩ.. 29

Figure 19. Model of partial winding of SERAPHIM motor testbed coil that shows axial coolant channels placed between alternate layers of winding. Space between layers without coolant is filled with thin fiberglass-epoxy composite prepreg to bond layers. 30

Figure 20. Resistance and resistance ratio of test coil of 380 turns of #8 square copper wire with mock radial gaps for coolant. Wire conductor size is 3.3 mm. Measured DC resistance is 500 mΩ. 31

Figure 21. One pancake coil layer with two of many spacers. The coolant flow path is proposed to be radial between the spacers, on the top of the pancake coil shown, and below the next pancake coil that would be mounted above.......... 33

Figure 22. The first radial wire layer upon the mandrel, and the start of the second radial layer. The spacers are placed during the winding process and create axial channels between each wire layer and adjacent spacers.......... 33

Figure 23. Coolant flow paths through a coil (the number of radial layers and turns per layer are reduced in the diagram for simplicity). 35

Figure 24. Lower coolant plenum geometry using round mesas. Each ring of mesas aligns with a layer of wire in the coil.......... 36

Figure 25. Pressure distribution in the top and bottom plenums. The break in the plot is the dividing radius. The pressure in the top plenum is not continuous at the dividing radius. 38

Figure 26. Axial velocity distribution in the axial channels. The break in the plot is the dividing radius. 38

Figure 27. Pressure distribution along a circumferential header for four feeds. 40

Figure 28. Initial coil concept that used coolant flow in the radial direction between stacked, pancake-type winding layers. 41

Figure 29. Finite element model of axial cooled motor coil.......... 42

Figure 30. Analysis process for merging Lorentz forces to an Exodus finite element model.......... 43

Figure 31. Bonding shear stress (psi) distribution of the lower coolant plenum to the bottom of the winding for a pure thermal load case (Case 3, Table 7).......... 45

Figure 32. Bonding tension stress (psi) distribution of the lower coolant plenum to the bottom of the winding for a pure thermal load case (Case 3, Table 7).......... 45

Figure 33. Bonding shear stress (psi) distribution of the lower coolant plenum to the bottom of the winding for combined loads (Case 4, Table 7). 46

Figure 34. Bonding tension stress (psi) distribution of the lower coolant plenum to the bottom of the winding for combined loads (Case 4, Table 7).......... 46

Figure 35. Bonding shear stress (psi) distribution of the lower coolant plenum to the bottom of the winding for combined loads (Case 5 in Table 7). Plots a and b use different maximum contour levels to show details. 47

Figure 36. Bonding tension stress (psi) distribution of the lower coolant plenum to the bottom of the winding for combined loads (Case 5, in Table 7). 47

Figure 37. Static testbed frame holds coils with their axis of symmetry in the horizontal plane. Relative positions of coils are variable.. 49

Figure 38. Power supply circuit to drive the motor coil for the static testbed................................ 49

Figure 39. Winding of sub-scale coil for the static testbed in the lower half of the housing body. Cables for fiber optic temperature and strain gauges are wrapped on coil mandrel. 50

LIST OF TABLES

Table 1. Parameters of Each Car of Notional Transit Consist. 12
Table 2. SERAPHIM Motor Performance, Normal vs. HTS 21
Table 3. Parameters of Normal Conductor Baseline Coils. 22
Table 4. Comparison of Results of Normal and Superconductor Motor Windings. 25
Table 5. Comparison of Full-scale SERAPHIM Motor Coil with Sub-Scale Coil for Static Testbed. 27
Table 6. Material Property Specifications for the Analysis of the Axial Cooled SERAPHIM Motor Testbed 43
Table 7. Stress Results Summary for Cases 1 Through 5 44
Table 8. Dynamic Load Estimates for 300 Hz Mechanical Vibration. 48
Table 9. Best Estimates of SERAPHIM Motor Coil Response Maximums Including Pressure, EM, Temperature, Vibration, and Wire Contact Area. 48

ACKNOWLEDGEMENT

The authors thank the efforts of our sponsors, Quon Kwan and Venkat Pindiprolu of FTA; David Keever, of SAIC; George Anagnostopoulos, Frank Raposa, and Marc Thompson of the FTA technical review team; Miller Hudson and Jack Stauffer from the Colorado Intermountain Fixed Guideway Authority, and Dr. Donald Rote of Argonne National Laboratory. We also thank Rachel Giunta, Stacie Hammerand, and David Zamora of Sandia's Organic Materials Dept. for their efforts in selection and test of adhesive systems, Dennis Muirhead and Pete Wakeland of the Pulsed Power Design and Development Dept. for their assistance in mechanical systems design, Gerry Wellman of Materials Mechanics Dept. for solid mechanics consultation, and Lance Thompson, Tim Coleman, and staff at Stangenes Industries for their efforts in coil fabrication.

INTRODUCTION

Previous Studies

The Segmented Rail Phased Induction Motor (SERAPHIM) is a type of linear induction motor that consists of air-core, discretely-energized motor coils capable of efficiently providing high thrust. These coils generate thrust by repelling passive, shorted coils in the guideway with clearances of several centimeters. With the potential for a low-cost guideway by the use of a wide clearance between vehicle and track coils, this propulsion system is being evaluated for urban maglev transit applications.

The SERAPHIM concept evolved from "coilgun" technology developed at Sandia National Laboratories for launching large and small projectiles at high speed [1,2]. Both technologies are based on the principle of sequentially energized coils creating a time-varying magnetic field and inducing a current in a shorted coil to generate a repulsive thrust. A notional, single-sided, single-coil SERAPHIM motor is shown in Figure 1. The motor coil is energized as it passes over a track coil to which it is well coupled. Current is provided from the time when the motor coil is centered over the track coil until the magnetic coupling diminishes at about a displacement of a coil radius. Continuous propulsion is achieved for a vehicle by using a multiple-coil motor where the coils are energized sequentially at an optimum position to provide thrust or braking as shown in Figure 2 and Figure 6. [3]

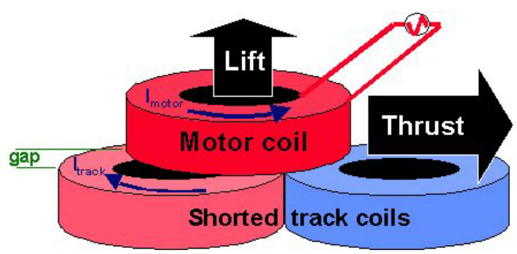

Figure 1. Basic SERAPHIM motor configuration using one motor coil and multiple track coils.

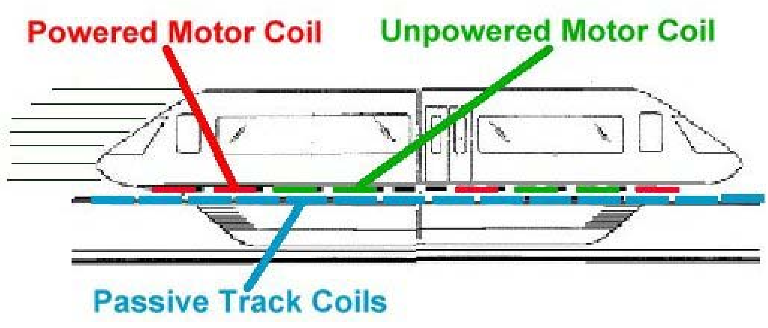

Figure 2. Each vehicle powered by 4-coil SERAPHIM motor. Red coils are powered at position shown. Green coils, presently unpowered, will be energized as vehicle moves them into optimum position for thrust.

Previous work with the SERAPHIM concept has established proof-of-principle testing and potential benefit from system studies. The original concept, which was developed in an internally-funded research project at Sandia National Laboratories in 1994, used solid aluminum plates instead of wound track coils to minimize guideway cost. A demonstration test was done where 3 pairs of track coils were held fixed and a 14.4 kg track plate was accelerated to 54 km/hr. This testing validated a magnetic field analysis code that was developed to analyze the coil's performance. Scaling was done with this code to project the performance of a 320 km/hr, SERAPHIM-powered, multi-car train supported on passive steel wheels. The analysis indicated that the cost of the system was comparable to that for steel-wheeled, high-speed rail, and provided the capability to climb grades significantly higher than the 6% grade limit for most conventional trains [4].

Another internally-funded study was conducted in 1999 to estimate system performance and develop concepts for a continuously-operated motor coil [5]. A simple, point-mass, dynamic-response spreadsheet model was created to simulate a train's performance over a specified route. A power supply and coil circuit code was also developed to model the electrical and mechanical performance of the motor. The use of a lumped-circuit-based model was now practical as analysis suggested improved performance with wire-wound coils in the track instead of solid plates. Finally, a basic concept was developed for the coil and power supply circuit for a 5-coil SERAPHIM motor to operate at speeds up to 216 km/hr. A very limited amount of analysis suggested the concept might be viable to propel a multi-car consist at highway speeds, but also indicated that further analysis was necessary to have self-consistent assessments of thermal management, mechanical stress, and electrical power.

Application to Low-Speed Urban Maglev

This present project has extended the previous studies in many important areas that has resulted in a SERAPHIM motor and power supply capable of propelling a potential urban maglev vehicle over a strenuous route. Using improved analysis tools, the design is self-consistent for thermal, mechanical, and electrical loads, which is a significant improvement over previous concepts. The motor coil and power supply have been fabricated for steady-state endurance testing in a static testbed that includes a cooling system, diagnostics to evaluate mechanical, thermal, and electrical responses, and a support structure. These tests will be conducted in the following phase of this project.

Specifically, this project has accomplished the following results:

1. Conducted analyses with the point-mass, dynamic-response spreadsheet model to establish potential performance for the motor and set requirements for thrust and power. The model was improved to include speed limitations based on route curvature, vehicle tilt, track superelevation, and lateral acceleration limits.
2. Evaluated with this model the thrust and power required to drive vehicles ranging in mass from 23 to 35 tonnes over a potential transit route in the Denver metropolitan area at speeds competitive to the adjacent highway traffic. Information from the Low-Speed Maglev Technology Development Program and the Colorado Department of Transportation I-70 Mountain Programmatic Environmental Impact Study (PEIS) was integrated into the model. We determined that motor power and thrust could be significantly reduced (factor of 3) from estimates made with the previous model due to reduction of vehicle mass and speed limitations required by route curvature.
3. Improved the SERTRAIN lumped-element circuit code to include options for the power supply configuration and operation, and coil geometry definition. The previous concept of using a fixed, 60 Hz frequency power supply was replaced with phase-controlled, variable-frequency inverters to minimize peak reactive power demand. Operation at higher frequency proves better than 60 Hz for efficiency of switching from coil to coil, but must be balanced against the increased size of the on-board resonant capacitors and the AC losses in the coil.
4. Developed analytic thermal design models that considered fluid flow and heat transfer in the coil as well as details and design of the components of the external heat rejection system. This tool allowed rapid evaluation of designs and the impact of constraints placed by the mechanical and electrical systems.

5. Developed a mechanical stress analysis model from the CAD drawing models, circuit simulations, magnetic field analysis, and thermal design tools. Complete coil and component models were used to evaluate impact of electromagnetic and thermal-induced loads and set requirements for materials selection.
6. Established the design requirements for powered vehicle coils, track reaction coils or plates, and power and cooling subsystems to achieve the competitive speed along the route by analysis with the electrical, mechanical, and thermal tools described above. This analysis resulted in the rejection of the early baseline coil design concept using radial cooling manifolds for mechanical support and heat transfer due to complexity, and developed a simpler coil designed with axial coolant flow. Likewise, the use of superconductors for the motor coils was assessed and rejected. This was due to the reduction in efficiency associated with the power to operate refrigeration systems to remove the heat generated by the AC losses in the high-temperature superconductors.
7. Designed a test motor for evaluation under static conditions in a testbed to verify magnetic forces and Ohmic losses. The nominal half-scale motor coil will be capable of steady-state operation at the mechanical, thermal, and electrical stress levels anticipated in the full-scale design. This testbed includes half-scale motor and track coils, inverter power supply, cooling system, diagnostics, and experiment controls. The testbed structure will allow testing of coils over a range of relative positions that simulate track load conditions.
8. Completed procurement of coils, power supply, and cooling system for the static testbed. Components are being delivered for the assembly and testing phase. The upcoming test data will provide an excellent benchmark for our motor design codes and allow accurate assessment of system performance.

DESIGN BASIS

A primary deliverable for this project is the design of a SERAPHIM motor sized to meet the system requirements of an urban maglev transit system for the Denver, Colorado region. Our Project Implementation Plan (PIP) identifies that the system could extend from Denver International Airport to the western suburbs as far as Evergreen [6]. This route, shown in Figure 3, has region of low grade within the city, but grades over 6% exist along Interstate-70 approaching the exit for Evergreen. Achieving an average speed of 112 km/hr that is competitive with traffic on the interstate under best weather and traffic conditions was highly desirable to ensure ridership on this route segment.

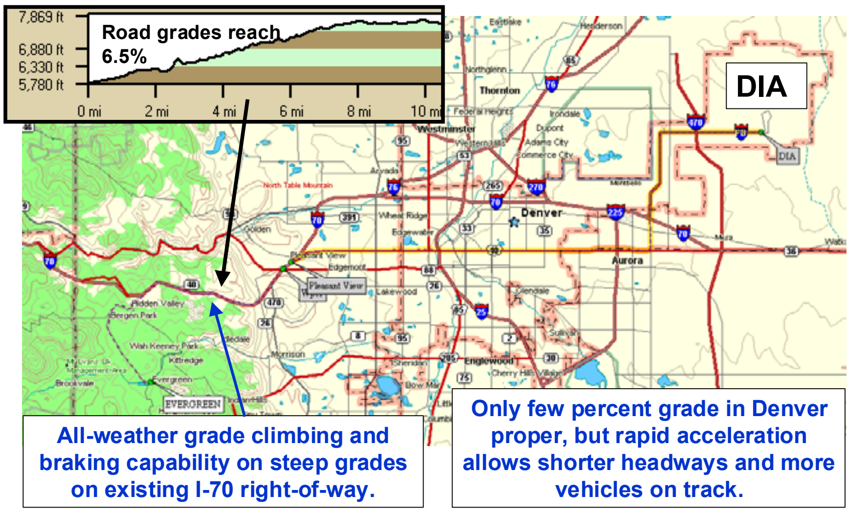

Figure 3. Potential route for maglev transit system in Denver metropolitan area. Test case route used to determine basis for coil design is along I-70 from Colorado 470 to the Hidden Valley exit.

Feedback at our preliminary system design review suggested that for this route, the vehicles in the range of 23 to 35 tonnes should be considered with the motor just having enough thrust for 0.15 g acceleration and achieve 112 km/hr average speed (including station dwell) climbing the test case route segment. With these changes, further analysis with the point-mass dynamic response model showed that the peak thrust and power of the motor could be reduced to 33% of that originally estimated from previous studies.

Table 1. Parameters of Each Car of Notional Transit Consist.

Length, width, height	7.6 m, 2.6 m, 3.3 m
Mass loaded	11.3 tonnes
Passengers per car	20
Motors per car	1
Coils per motor	4, 2 operating simultaneously
Maximum acceleration	0.15 g
Maximum speed	160 km/hr
Station dwell time	0.5 to 2 minutes
Average speed including stop	50 km/hr or greater
Curve superelevation	15°
Max lateral acceleration on curve	0.1 g
Average thrust per motor	16.5 kN
Average mechanical power per motor	273 kW
Electrical to mechanical efficiency	50% average over route
Motor-to-track clearance	2.5 cm

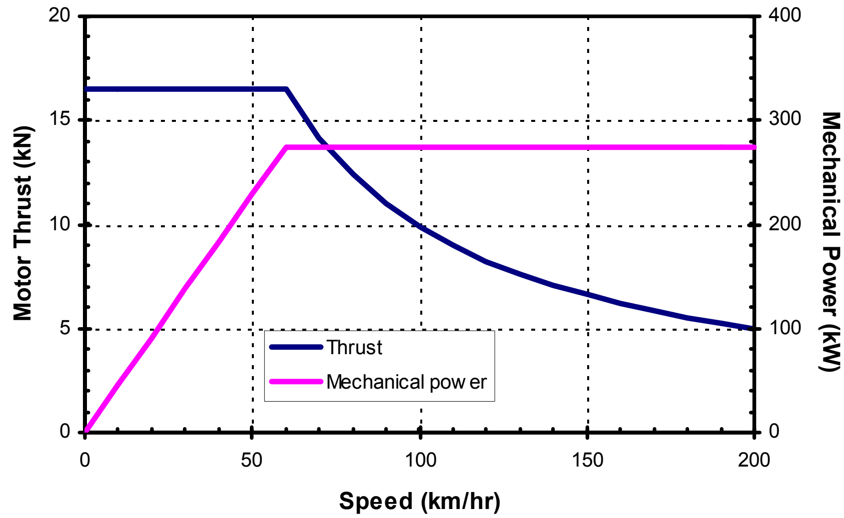

Figure 4. Typical thrust versus speed curve developed for SERAPHIM motor to achieve high thrust at low speed, then decreasing inversely with speed above a critical speed that sets a maximum mechanical power.

The proposed design is a four-coil SERAPHIM motor powering a two-car consist similar to that shown in Figure 2. The parameters for each car of the consist given in Table 1 represent a notional vehicle with operating parameters based on maglev top-level system requirements that could be utilized in several locations [7].

Dynamic propulsion analysis was conducted with a spreadsheet model using equations which include 1) vehicle size and mass, 2) effects of road grade, elevation, and vehicle drag, 3) speed limits determined by maximum allowed longitudinal and centrifugal acceleration from superelevation and route curvature, and 4) motor thrust versus speed curves and efficiency. Given the constraints of a vehicle and a route, the thrust curve is determined that is necessary for the motor to meet the route's required average speed. The shape of a typical thrust curve is shown in Figure 4 where the motor is operated at a constant, maximum thrust up to a "critical speed" above which the thrust is scaled inversely with speed for operation at constant mechanical power.

The route selected as a test case for the design was along a 14 km mountainous section of Interstate-70 extending west of Denver, Colorado. This segment represents a strenuous section of a possible future metropolitan transit system [8]. The route contains a long continuous elevation climb shown in Figure 5 with regions of 6.5% grade. Numerous curves with radii of curvature on the order of 350 - 390 m exist along the highway right-of-way causing the maximum speed limit to be reduced to limit lateral acceleration. The speed limit profile shown in Figure 5 is based on a 160 km/hr maximum and the values in Table 1.

A four-coil SERAPHIM motor with thrust and power curves as shown in Figure 4 powering each car of a two-car consist results in a speed profile as shown in Figure 5. Four coils per motor were proposed with 2 operating simultaneously to distribute the load within the motor and smooth the acceleration. Analytical scaling showed that the coils could be smaller diameter that previous 1 meter diameter concepts. This analysis set the specification of average thrust for each of the four, 0.8 m diameter coils operating at 50% duty factor at 8.3 kN with the mechanical power held at 137 kW at speeds greater than 60 km/hr.

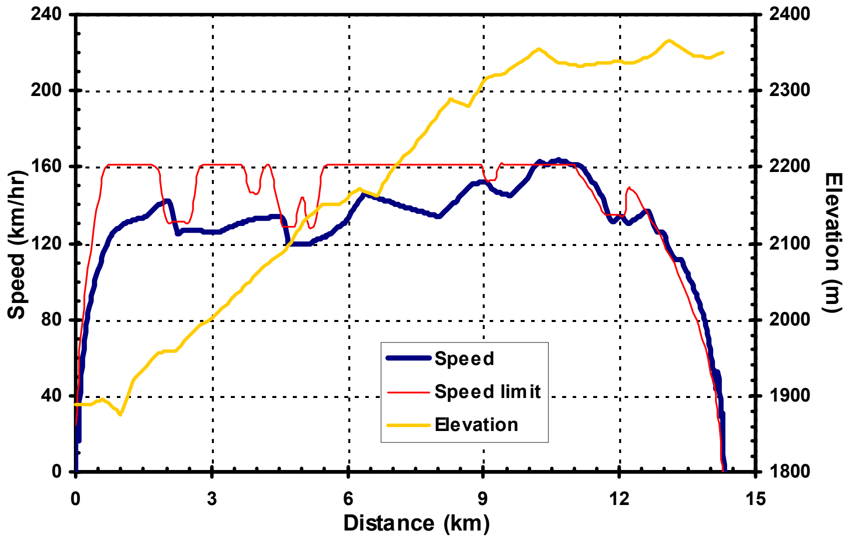

Figure 5. Elevation profile and speed limit for route segment used to determine motor thrust and power requirements.

MOTOR CONCEPT AND PERFORMANCE CALCULATIONS

A SERAPHIM motor has one or more on-board, powered motor coils and passive, shorted coils in the track. A four-coil motor concept is shown in Figure 6 where two of the four coils are operated simultaneously to smooth acceleration and distribute the thrust load. Which of the four coils is energized is controlled to provide the optimum thrust (or braking) and is dependent upon the position of the motor's coils over the track coils. Each of the energized coils is powered by one of two variable-frequency inverters and resonant capacitors. Power for the inverters is shown to be high-voltage AC picked up from a hot rail or catenary along the track, but on-board power generation is also an option.

The analysis of the motor performance is based on our lumped-element circuit code, SERTRAIN, which calculates the thrust and lift forces on the individual coils of the motor. These forces are based on the self-consistent transient current response in the motor and track coils due to a time-dependent voltage forcing function applied from the inverter, as shown in Figure 6. Where appropriate, the calculation can be divided into the response of individual motor coils with one or more track coils as shown in Figure 7. Coil self and mutual inductances and resistances are calculated based on input geometry, coil relative positions, and materials properties. Resistance is also adjusted with the temperature of the conductor during the calculation. The efficiency is determined from the calculation's energy balance comparing change in kinetic energy to input energy. The analysis can be done with a vehicle point mass to calculate acceleration/deceleration or at constant velocity. Parasitic couplings to other structures can also be added.

Figure 6. Block diagram of circuit driving a four-coil SERAPHIM motor, where the on-board

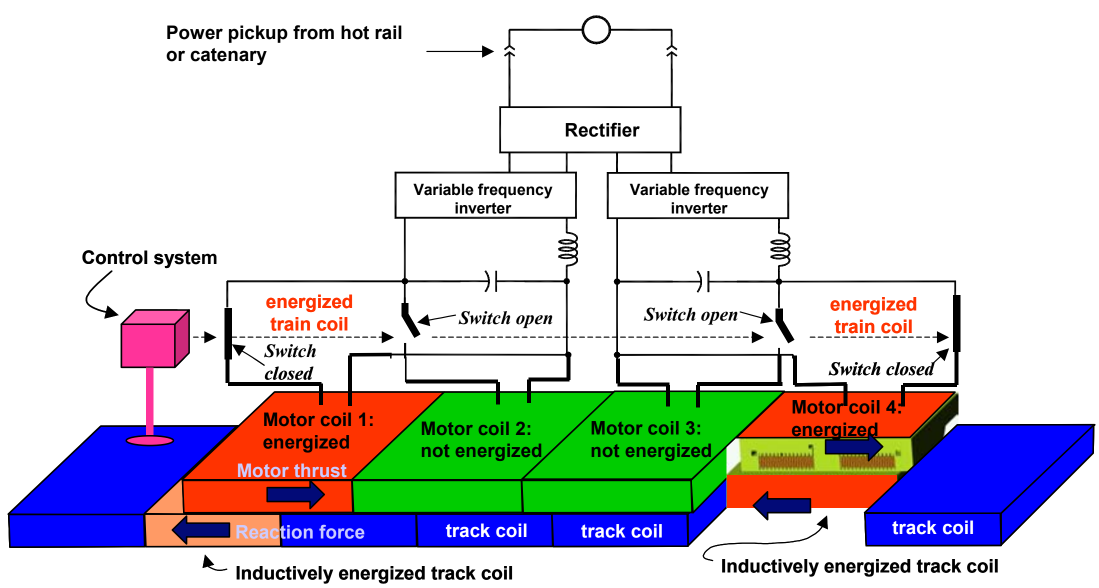

motor coils are switched sequentially to the inverter-capacitor power supply to provide optimum thrust or braking.

The SERTRAIN lumped-element circuit code was significantly improved in this project to include options for the power supply configuration and operation, and coil geometry definition. Earlier code versions used fixed frequency power supplies only. The previous concept of using fixed, 60 Hz frequency power supply was replaced with phase-controlled, variable-frequency inverters to minimize peak reactive power demand and improve efficiency. Ideally, the inverter should only provide the average power associated with ohmic losses and mechanical thrust. The capacitor is to deliver the reactive power associated with energy oscillating between it and the coil. Other modification to the code allowed the analysis of a motor coil with multiple track coils and other motor coils.

The full-scale coil has been designed for the motor to meet the transit route specification of 8.3 kN average thrust per coil. This coil, similar to that shown in cross section in Figure 5 has an 80 cm outer diameter, 42 cm inner diameter, and 7 cm height. The winding consists of four #8 square copper magnet wires in parallel, each making 230 turns. These parallel wires are transposed periodically in the winding to equalize the current distribution. With a 27 kV peak voltage applied at a nominal 150 Hz resonant frequency from the inverter, a peak current of 1 kA circulates in the drive coil and 0.6 kA in the 370 turn track coil at maximum coupling. Physical spacing between motor and track coil is 2.5 cm and the windings of these coils are spaced about 4 cm. The center-to-center spacing between motor coils is 1.25 times the motor coil diameter and the track coil spacing is equal to that coil's diameter.

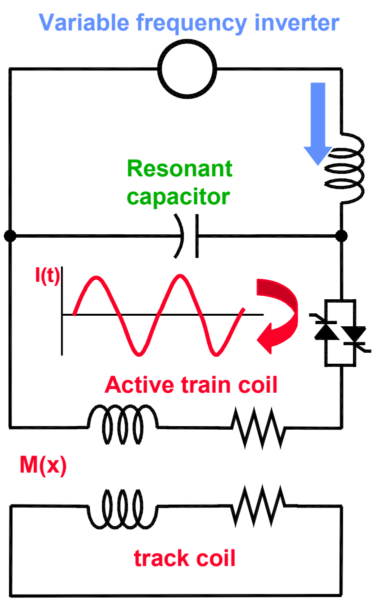

Figure 7. One of several motor coil and track circuits analyzed by the SERTRAIN code. The transient, coil current response is calculated based on the variable frequency voltage forcing function from the inverter applied to the resonant capacitor-coil(s).

A feature of the operation of the motor is that the switching of the +/- voltage of the inverter is synchronized with the voltage oscillation across the capacitor. This keeps the inverter frequency and voltage in phase with the resonant response of the capacitor-coil circuit. The capacitor then maintains the same peak voltage in every oscillation cycle despite the change in resonant frequency due to the changing mutual inductance to the track coil. When thrust diminishes in one energized motor coil, the capacitor is switched at peak voltage to another motor coil at a time the current crosses zero in the low thrust coil. No current flows in the first coil again until another track coil is well coupled at a position to provide thrust.

The goal to minimize the mass and volume of the on-board power supply and power conditioning equipment led to a significant effort (delaying the original PIP date for the Initial Design Review about three months) into the development of the phase-controlled inverter power supply circuit to minimize the reactive power demand on the inverter. Previous concepts considered such as driving the coils with fixed frequency were not acceptable. Additionally, the choice of resonant frequency was considered a tradeoff between the mass of the resonant caps, which scale with frequency and the impact on the efficiency of the motor due to non-optimum switching the capacitor from coil-to-coil at low frequencies. A resonant frequency of 200 Hz was selected in this compromise.

Circuit analyses were conducted with the SERTRAIN code at several vehicle speeds to determine motor performance. Figure 8 shows an example output of the applied inverter voltage, the response input current, and the voltage response across the capacitor during the interaction of one motor coil and track coil at 144 km/hr. The peak value of the capacitor voltage oscillation is maintained at the value of the inverter output while the coil is energized by optimization of when the inverter voltage polarity is switched. Figure 9 shows the resulting instantaneous and average thrust and lift forces from that same interaction. The abscissa values are the displacement between the centers of the interacting motor and track coil. Typically, the motor coil is energized from when the centers are slightly offset until the motor coil is displaced about a distance of a coil radius which in this case is on the order of 0.4 m. The lift force is significant since the motor is single-sided and configured horizontally above the track coils to produce this force. Double-sided configurations where two motor coils straddle vertically-oriented track coils are feasible and are being considered [3].

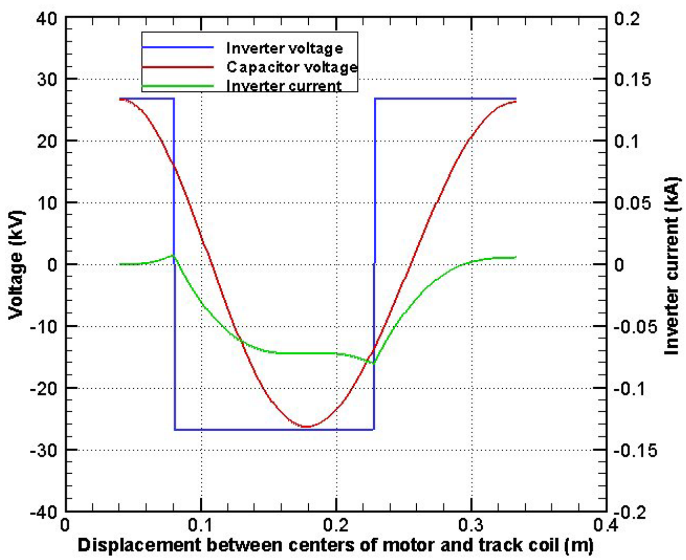

Figure 8. Polarity of applied voltage from inverter is synchronized with voltage across the capacitor so the capacitor maintains the same peak value in each oscillation cycle, and provides the same power when switched to another motor coil.

The efficiency of the SERAPHIM motor determined from calculations described above is shown in Figure 10. This efficiency is the value at the power pickup from the hot rail or catenary, and it includes estimated losses in all motor and track components as well as an assumed efficiency of 90% for the rectifier/inverter. Considering the vehicle speed profile shown for the route in Figure 4, the motor efficiency is estimated to exceed 50% over most of the route. Additional improvement is expected when optimized motor control for the route is taken into account. The coil size and spacing within the motor were sized to ensure a maximum operating speed of 160 km/hr (100 mph). If route curvature and acceleration limits preclude utilizing this speed capability, the motor design would be modified to shift the peak efficiency closer to the maximum operating speed. These changes may involve a reduction in coil diameter and input power if consistent with the peak thrust requirements and maximum coil stress. The static testbed described below will provide the basis for further optimization. The maximum efficiency of the SERAPHIM motor at 160 kph is within a few percent of the maximum efficiency of the Japanese HSST-100 driven by a conventional linear induction motor designed for a maximum speed 110 kph. However, at low speeds (35 kph), the efficiency of the SERAPHIM motor is lower than that for the same LIM, which has been optimized for the lower operating speed.

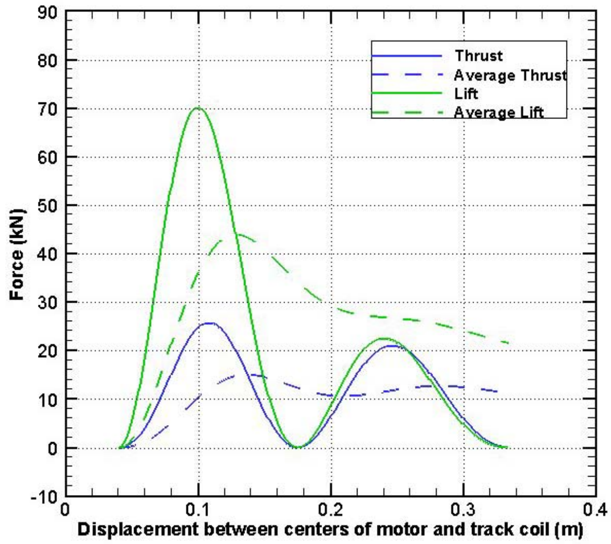

Figure 9. Instantaneous and time-averaged thrust and lift forces from interaction of a single motor and track coil. Although the coil has a radius of 0.4 m, the power is switched to a different coil at 0.33 m at the time of zero current in the motor coil.

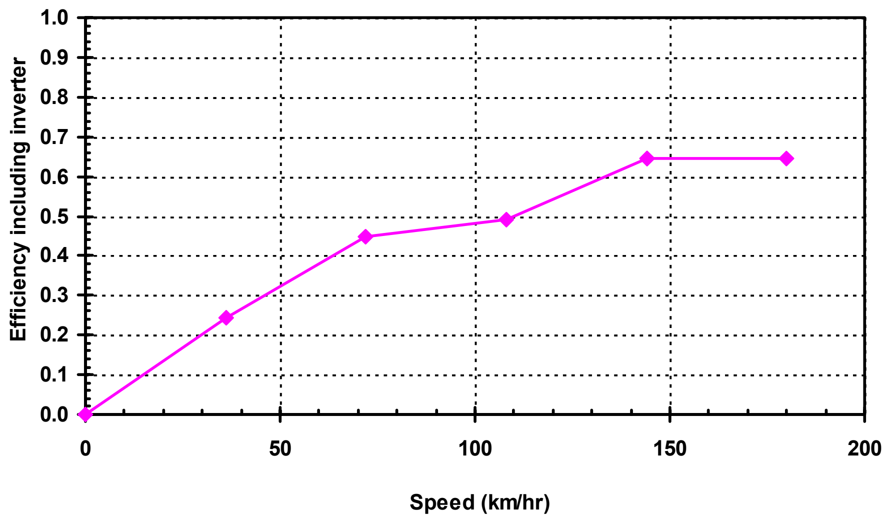

Figure 10. Average efficiency of full-scale motor at power pickup calculated with SERTRAIN circuit code, including an estimated 90% efficiency for the rectifier/inverter.

SUPERCONDUCTOR OPTION FOR THE SERAPHIM MOTOR

The Promise of Superconductivity

Superconductivity is the movement of charge through a conductor with zero, or negligible resistance. Large electromagnets require significant electrical currents through long runs of wire. By using superconducting materials, the losses associated with Ohmic heating can be reduced or eliminated.

The use of superconductive materials offers another significant advantage. To make high magnetic field electromagnets, the wire needs to be relatively small so that a significant number of turns can be located within a specified volume. Superconductive wires can be made much smaller than conventional wires of the same capacity. Thus, the magnet can be made smaller and lighter, and potentially the power supply weight can be reduced. The advantages of a reduction in weight of a transportation system are obvious. Yet there are other advantages. A smaller magnet can mean fewer materials to purchase, and fewer materials to machine.

The Problems of Superconductivity

Whereas superconductivity offers great promise, it is not free of complexity. First, the material has to be very cold. Since the required temperature is below ambient, the cooling system must include a refrigeration cycle, which will consume more energy than the typical coolant system for a conventional magnet. Also, the required cryo-refrigeration equipment may reduce the reliability of the system. Cryo-refrigeration equipment is complex, and its use on a moving platform could reduce its reliability.

The cold material will have to be insulated from the environment to minimize the power required by the cryo-cooler. Vacuum insulation is typically employed. Introduction of a vacuum insulation system may result in a larger electrical gap between the motor and track coils, which would reduce the system efficiency.

The insulation system makes it difficult to extract asymmetric thrust and lift forces from the cold magnet structure. Any structure that attaches the magnet to the train will result in a conductive heat leak that bypasses the insulating vacuum. This problem also exists in MAGLEV applications which use a DC superconducting magnet on the vehicle.

Also the superconducting material can be quite expensive. Thus, one would not consider using it at this time for the track coils, for one track coil is installed in each meter of track. Finally, the system has to be designed to withstand a cooldown to cryogenic temperatures. Differential thermal expansion of the various components can introduce significant stresses within the system.

Analysis of Effect of HTS on System Efficiency

At this point in time, much of the information about the performance of superconductive materials is proprietary. This is especially true for their performance in AC applications. Thus, it is not possible to determine the cooling requirements from first principles for our application. The performance of High Temperature Superconductor (HTS) materials in the SERAPHIM motor coil will be determined by comparison to one of the proposed HTS applications in an AC environment [9,10,11].

Waukesha Electric Systems has teamed with Intermagnetics General Inc. to design a HTS transformer. This transformer operates at 60 Hz with a peak magnetic field of 0.1 Tesla. The goal of the project is to produce a transformer that has reduced electrical losses, is smaller and lighter, and allows for greater overdesign performance.

The designers claim that the electrical power to run the cryo-cooler for this system is 0.1% of the transformer rating. They also claim that the losses scale with frequency and magnetic field. The transformer generates significant internal forces, but they are balanced and do not have to be extracted to the warm environment (except for the weight of the machine). So the conductive heat leaks into the transformer may be less than what will be experience by a superconductive motor coil.

Many applications of superconductivity use DC current. This is because the Ohmic losses can be essentially zero. However, due to the nature of the material, the losses are not zero during AC operation. Scaling laws can be obtained to scale the AC losses to different frequencies and magnetic field levels. Mike Walker (of Intermagnetics General) claimed that the AC losses increase with frequency. He claimed that this increase is proportional to the frequency to the first to second power depending upon the material and magnetic flux level. He also said that the losses scale with the magnetic flux level to the first to third power.

We have assumed that we can scale the cryo-power requirements of the transformer to our motor coil using the above scaling laws. We have optimistically assumed that the magnetic coupling between the motor and track coil will not change due to the introduction of a vacuum insulation system. We have optimistically assumed that the AC losses scale with frequency to the first power and magnetic flux level to the first power. Our motor operates at a frequency of 200 Hz, and a magnetic field of 1 Tesla. This results in a cryo-cooling power of 3.3% of the circulating coil power (14 MW). Thus, our peak refrigeration power would be 450 kW.

From this simple calculation we see that the elimination of the normal conductor Ohmic losses, which were only on the order of 1% of the circulating power, results in a much a larger drain on our system. Thus, the efficiency of our system actually decreases by using a HTS coil.

Analysis of Effect of HTS on System Performance

We have examined the effect of the use of HTS for the motor coil on system performance. Since the coils are lighter than conventional coils, the weight savings may provide an advantage. And since the Ohmic losses may be smaller, and the magnetic coupling could increase, we could possibly also use a smaller power supply to obtain the same thrust levels. Figure 11 compares the efficiency of a standard SERAPHIM motor to one using lossless HTS coils. This figure shows the potential savings of replacing the motor coils with HTS. However, these results ignore actual losses associated with AC operation and the electrical inputs of the cryo-cooling system that will be required by the HTS coils.

Table 2 shows a more detailed comparison of the SERAPHIM system using a normal coil (early design) and a HTS motor coil. The superconductive coil can be made with a smaller height since the wire size is significantly smaller. The peak field level and the average thrust are maintained. The lower losses in the HTS coils (we have assumed zero losses for this simple comparison) results in a lower peak source current and a lower coil current peak. The HTS coil cryo-cooling system requires a significantly greater electrical power than the simple coolant pump provided the conventional coil. When one includes the energy costs of the cryo-cooling system, it is seen that the efficiency of the HTS system is significantly lower.

Table 2. SERAPHIM Motor Performance, Normal vs. HTS

	Normal Conductor		**Superconductor**	
Coil height (cm)	7		1	
Peak field level (Tesla)	1		1	
Source current peak (A)	130		66	
Coil current peak (A)	2500		2200	
Coolant temperature (C)	45		-240	
Max. thrust/motor (kN)	16.6		16.4	
Diameter (m)	0.8		0.8	
Critical speed (km/hr)	72		72	
Ave. mechanical power (kW)	330		330	
Ave. cooling elect. power (kW)	0.06 (pump)		900	
Ave. electrical power (kW)	720		445	
Efficiency at 72 km/hr	0.46		0.25	
	Mass	**Volume**	**Mass**	**Volume**
Component	**Pounds**	**Cubic ft.**	**Pounds**	**Cubic ft.**
Motor drive	2200	110	1300	70
Charging inductors	290	3.6	180	2.2
Resonant capacitors	2000	41	1600	41
Motor coils	2000	12	720	12
Cooling system	400	6	2100	56
Total per car (4 motor coils)	6900	180	5900	180
Fraction of vehicle weight	0.28		0.24	

Table 2 also shows that the expected weight savings of a superconducting coil are not very large. This is because of the weight required by the cryo-cooling system. The amount of heat that has to be rejected actually increases due to the poor Carnot efficiency of the cryo-cooling system.

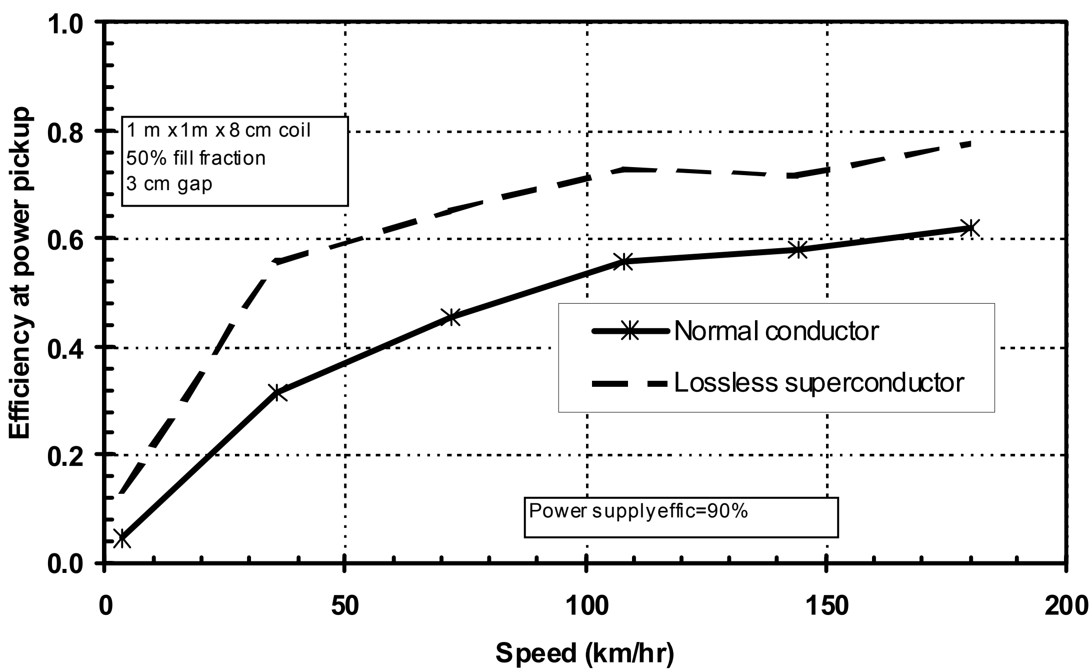

Figure 11. Comparison of lossless HTS to normal motor efficiency ignoring electrical requirement of cryo-cooling system. The calculation assumes the power supply efficiency is 90%.

Analysis of Motor Coil Performance with Superconducting Winding

Circuit analysis was performed with the SERTRAIN circuit code to simulate the performance of a SERAPHIM motor coil with a superconductor wire to compare with the performance of normal copper conductor as a baseline. The location of the motor coil within the motor housing is varied to determine the effect that the space for vacuum thermal insulation and mechanical support would have on motor performance.

Baseline case: Normal conductor

Although the SERAPHIM motor may consist of many coils, the effect of a superconductor wire can be evaluated from the performance of a single coil. The baseline normal-conductor geometry for the motor and track coils is shown in Figure 12, and the parameters of the coils are shown in Table 3. These values were determined from a design study where the required average thrust is 8.3 kN and coil temperature is minimized through tradeoffs in heat transfer and wire ohmic losses.

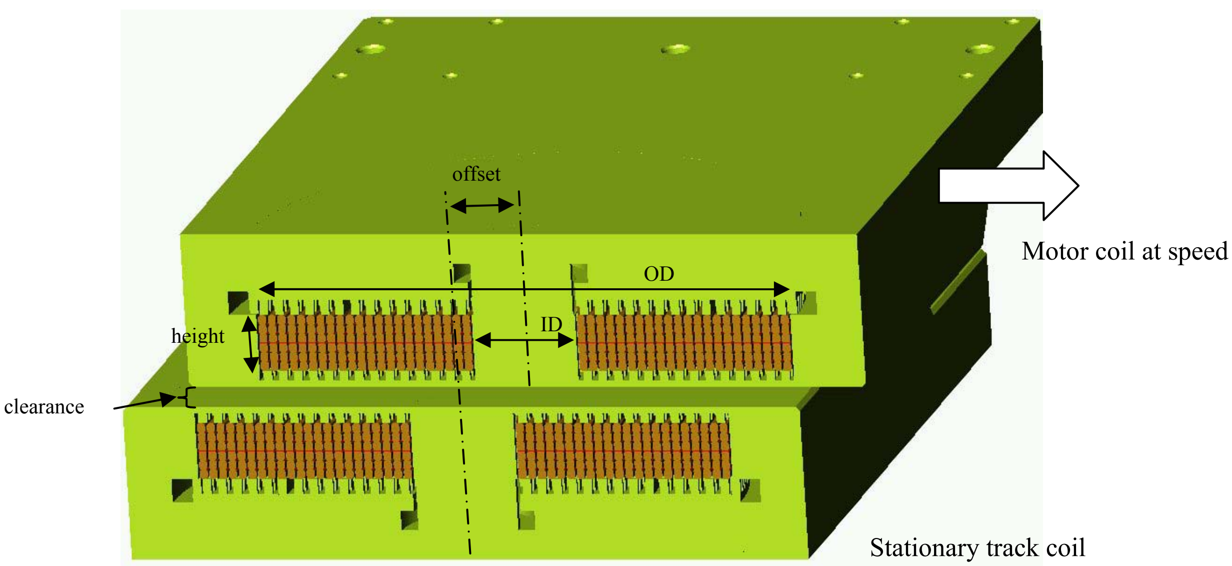

Figure 12. Geometry of baseline normal-conducting winding motor and track coil.

Table 3. Parameters of Normal Conductor Baseline Coils.

Parameter	Motor coil	Track coil
Winding inner diameter (m)	0.16	0.16
Winding outer diameter (m)	0.8	0.8
Winding height (m)	0.073	0.073
Winding material	Copper	Aluminum
Turns	132	156
Temperature (deg C)	100	100
Clearance (m)	0.0254	
Coil center-to-center offset at current switching (m)	0.04	
Motor coil speed (km/hr)	72 for this baseline analysis	

These parameters were input into our Fortran-based, lumped-element circuit code, SERTRAIN, which models the transient electrical response of a motor coil driven by a power supply and determines the mechanical forces from a motor and track coil system. Coil self and mutual inductances are determined from the input parameters and relative displacement of the coil centers. Circuit parameters are shown in Figure 13. The calculated time-dependent responses include: voltages, currents, power, energy, magnetic coupling, thrust and lift forces, ohmic heating, and electric-to-mechanical conversion efficiency. Peak values of currents are shown in Figure 12.

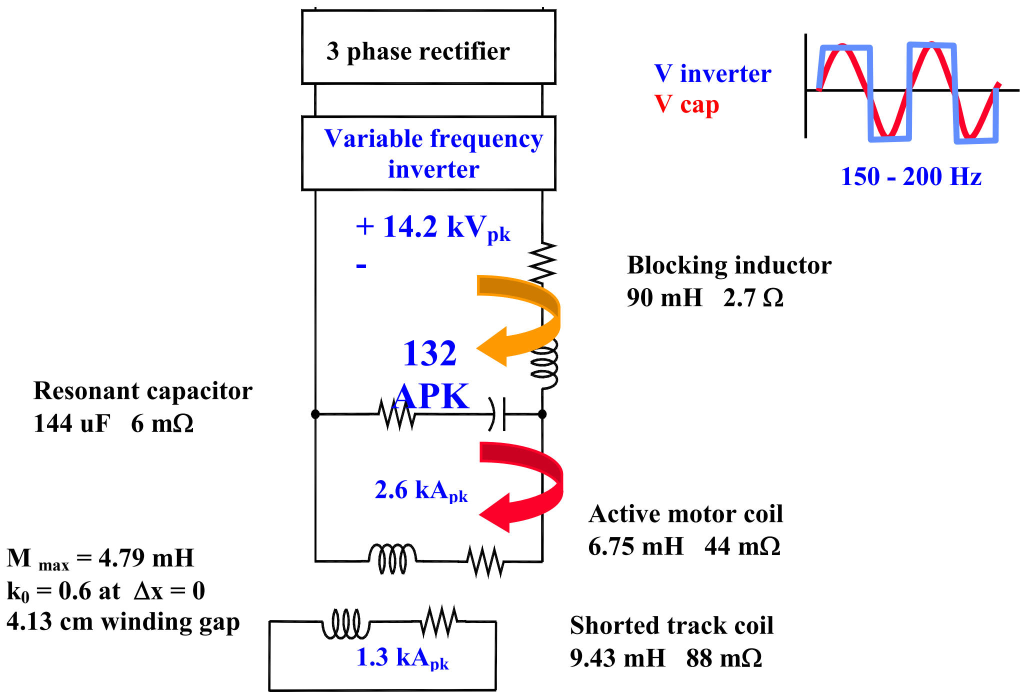

Figure 13. Diagram of circuit modeled for normal conductor baseline case.

The circuit analysis was performed for a motor speed of 72 km/hr, which is the highest speed at full thrust under the constraint of constant mechanical power. The analysis is conducted from an initial position where there is a small offset between motor and track coil centers to a position where the motor coil has moved a distance roughly equal to the radius of the track coil at which the thrust reduces to near zero. For a multi-coil motor, power would be switched to another motor coil that is in a more optimum position relative to its nearest track coil to provide thrust. Figure 14 shows the response of motor, track, and source currents as the motor coil traverses across a track coil. Current to the motor coil is switched "on" when there is an offset of 0.04 m and would optimally be switched off at 0.375 m. For the purposes of this graph, the current was allowed to flow until an offset of 0.5 m.

The average force generated by the normal conductor motor coil moving at 72 km/hr over a distance of 0.38 m is 8.3 kN with an average input power of 341 kW. This yields an electrical-to-mechanical conversion efficiency of 49%. The average ohmic power dissipated in the motor coil is 103 kW.

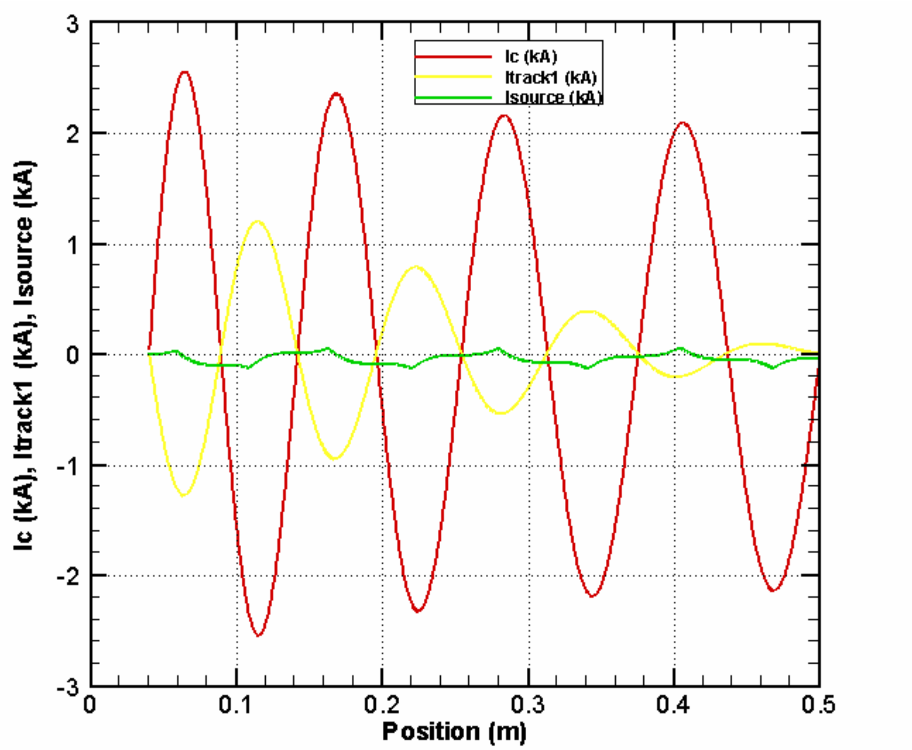

Figure 14. Current histories for motor (Ic) and track coils and inverter output current (Isource) feeding resonant capacitor. Position shown on abscissa is displacement between centers of motor and track coil.

Superconductor cases

Superconducting wire was only considered for the motor coil due to the prohibitive cost associated with applying to the numerous track coils. Because of the ability of superconductors to operate at greater current density, the height of the superconducting winding was reduced to one sixth the height of the normal conductor winding while maintaining the same number of turns. This is a conservative increase to allow for structure to reinforce the winding, and the resulting current density is well below (5 times) the critical current density limit for superconducting operation at fields of 1 Tesla and 40°K [9].

As in the case of the normal conductor winding, physical structure is needed to couple the non-symmetric mechanical thrust and lift loads generated within the winding to the room-temperature outer housing. Additionally, for the superconductor case, a vacuum space must be provided for thermal insulation. The addition of this space between the motor and track coil windings causes a decrease of magnetic coupling which results in lower induced currents in the track coil and hence less thrust.

To quantify the effect of this decoupling, three superconducting cases were evaluated with the motor coil placed at different positions within the motor housing. These are shown in Figure 15 overlayed on the location of the normal conductor. Position A is an extremely optimistic location given that the winding is in direct contact with the housing wall and assumes that sufficient cooling can be achieved from the top surface. This position, however, has the best magnetic coupling to the track coil and would provide the best performance. Position B is more probable with space allocated on both sides of the winding for load transmission structure and vacuum insulation. Position C is evaluated to determine the effect if additional space is needed. Should the winding be placed in this location, it is assumed the housing height would increase as necessary for similar space required above the winding.

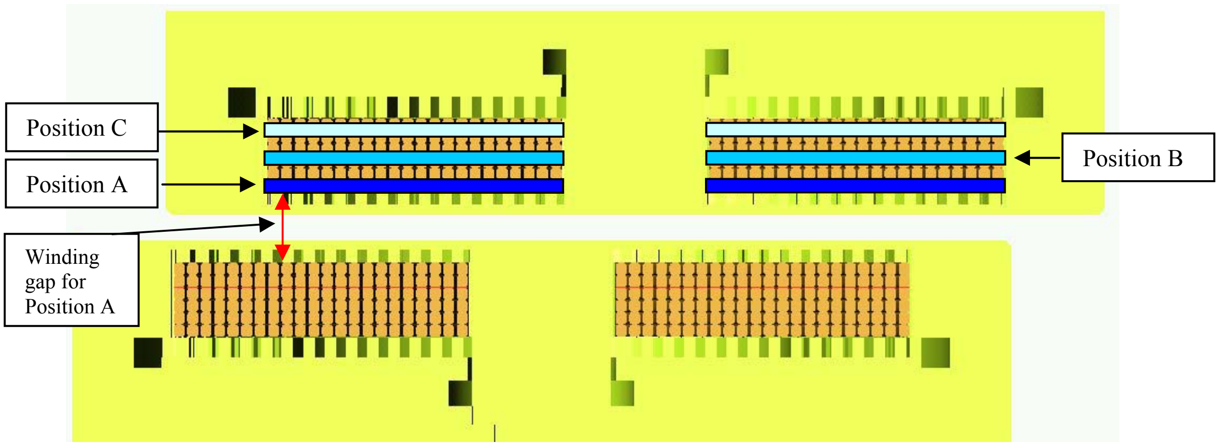

Figure 15. Possible positions, A, B, or C, of superconducting motor coil winding within housing.

Analysis with the SERTRAIN code was done for each of these cases with the following assumptions. Since the AC losses in the superconductor are so small, a zero resistance is included in the circuit analysis. However, the ohmic losses in the motor coil winding are accounted for by the peak circulating power and the efficiency of 3.3% of this power required for refrigeration. This efficiency is based on coil operation at 200 Hz and 1 Tesla magnetic field levels as discussed earlier. The resonant bank size and energy was adjusted so that the same average thrust of 8.3 kN at 72 km/hr was achieved for each motor coil position. These results are shown in Table 4.

Table 4. Comparison of Results of Normal and Superconductor Motor Windings.

					Average Power (kW)				
	V cap pk	Capacitor Bank		Winding	Motor coil	Inverter	Refrigerator	Total	Pmech/Pinput
Case	kV	uF	MVAR	gap (cm)	Ohmic	Output	Input	Input	Efficiency
Normal	14.2	144.4	18.3	4.1	103	341	0	341	0.49
SC case A	12.8	139.1	14.3	4.1	0	214	470	684	0.24
SC case B	17.7	114.8	22.5	7.2	0	216	742	958	0.17
SC case C	22.9	102.4	33.7	10.2	0	252	1113	1366	0.12

The calculations show that as the distance between the motor and track coil winding increases, the size of the bank must increase which is a measure of the increase in circulating power necessary to achieve the required thrust. This increases the AC losses in the superconducting coil and requires a larger bank to be carried onboard the vehicle. Even using the most optimistic position A for the motor coil winding, the total efficiency, when refrigeration power is included, is half that achieved with a normal conductor. The low efficiency for the more probable winding position B shows that the AC losses in the superconductor increase significantly as the distance between the motor and track windings is increased.

Summary and Conclusions on Superconductivity

It is determined that the use of HTS materials in the SERAPHIM motor coil does not increase system performance. This is consistent with the current list of proposed applications of superconductive materials. At the present time there is only one commercial application of superconductive materials in a high power application, which is a MRI magnet. This is a DC operation, and the use of superconductive materials has provided a significant improvement on the power consumption of the magnet.

Other proposed applications of HTS materials are also DC applications. These include electric motors (where the AC stator is a normal conductor and the DC rotor is made of HTS), superconducting magnetic energy storage (SMES), and MAGLEV trains.

There are a few proposed power applications of HTS, but they are lower magnetic fields and lower frequencies than required by the SERAPHIM motor coil. These include AC transmission lines, the transformer mentioned above, and a fault current limiter.

At a recent program review, it was suggested that Sandia investigate the HTS magnet developed by American Superconductor for minesweeping applications [12,13]. However, this magnet was only tested at 0.1 Hertz and 0.1 Tesla with an AC amplitude of only 30% of the mean. Thus, it was thought that the transformer used for comparison was a much closer match to the SERAPHIM motor. However if we apply the same scaling procedure using AC loss measurements from this device we find a refrigerant load of 1.5 MW for the SERAPHIM motor (even higher than our result using the transformer analogy).

In conclusion, use of HTS at high frequency and high field is not currently feasible due to AC losses. As materials improve, it may be possible to use superconductive materials in the SERAPHIM motor in the future.

COIL DESIGN

Two coil concepts were developed during the initial design of the motor coil for the static testbed: 1) the full-scale coil capable of meeting the system design requirements, and 2) a nominal half-scale coil capable of validating the design methodology, construction techniques, and performance at equivalent mechanical and thermal stresses. The sub-scale coil was chosen for the static testbed to minimize total cost for coils, power supply, and cooling systems. SERTRAIN code analyses, analytical thermal models, and scaling relationships provided the justification for maintaining the equivalence of thermal and mechanical stress between the two designs whose parameters are shown in Table 5.

Table 5. Comparison of Full-scale SERAPHIM Motor Coil with Sub-Scale Coil for Static Testbed.

Parameter	**Full-scale**	**Sub-scale testbed**
Winding diameter, height	80 cm, 6.8 cm	38 cm, 3.4 cm
Wire size (AWG), turns, # parallel wires	#8, 230, 4	#8, 380, 1
Distance between motor and track coil windings	4.1 cm	2.5 cm
Physical clearance between motor and track coil housings	2.5 cm	0.3 cm
Peak coil voltage	26.8 kVpeak	8.3 kVpeak
Peak coil current	1.08 kApeak	0.485 kApeak
Max Ohmic power dissipated in motor coil at 100% duty factor	137 kW	96 kW
Duty factor	50%	15%
Max wire temperature at duty factor	95°C	99°C
Max instantaneous thrust force	30.4 kN	6.5 kN
Max instantaneous lift force	85.9 kN	25.2 kN
Peak thrust/coil edge area	56 N/cm^2	50 N/cm^2
Peak lift/coil face area	17 N/cm^2	22 N/cm^2

The power level for the sub-scale coil was adjusted to achieve the same equivalent applied mechanical stress as the full-scale coil. Justification for proportional scaling is done by taking the thrust or lift and dividing by the respective coil surface area bearing that load. However, the duty factor for the sub-scale coil must be reduced to maintain the same wire temperature as the full-scale design.

The sub-scale coil designed for the static testbed shown in Figure 16 consists of a multi-layer winding embedded in a dielectric housing that provides mechanical support and distributes coolant to the winding. The single-wire winding has been structured with spacers between alternate radial layers for convective heat transfer from the wires to the coolant. Sub-scale coils will be configured in a static testbed geometry similar to that shown in Figure 1. While the position of all coils is fixed during testing, the coils can be tested in different positions relative to each other to evaluate a range of loading conditions.

The design shown in Figure 16 was the result of several iterations of the geometry of conductor and coolant passages. Early designs considered radial coolant flow paths, but the highly convergent flow near the inner diameter of the coil was problematic. That region of the coil was further complicated by the high density of axial wire transitions between the pancake layers of the winding in a region of high mechanical stress. These issues were mitigated by building the winding with axially symmetric layers that accumulated in the radial direction.

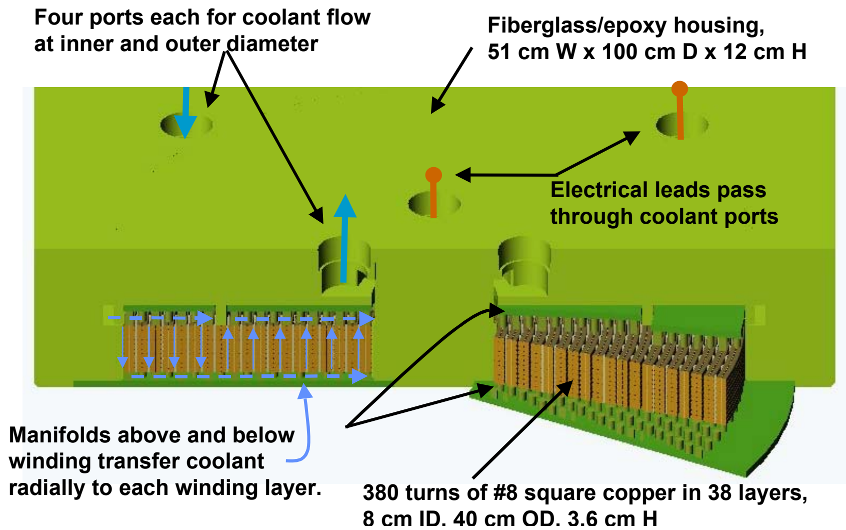

Figure 16. Cutaway of sub-scale coil designed for the static testbed.

Measurement of Coil Losses

The early design concepts used a relatively large wire size and proposed to operate at an inverter frequency of 200 Hz. A test coil was prepared with the same wire size (#3 AWG square, 0.58 cm conductor, 0.59 cm overall), inner diameter (8 cm), and number of layers (22) to measure the actual AC losses. The coolant channels were not added to minimize complexity which reduced the coil radial build and slightly increased the AC to DC resistance ratio. The resulting outer diameter was 34 cm. Six turns per layer were planned, but the winding construction yielded 5.8 due to the radial transition the wire must make between layers. While the coil maintained the originally planned 3.94 cm height (axial direction), the winding totaled 128 turns. A photo of the coil is shown in Figure 17.

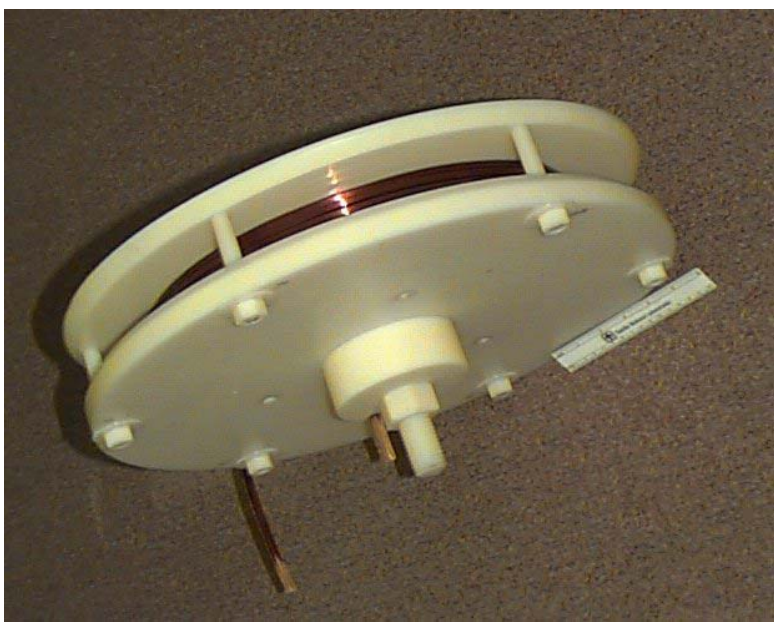

Figure 17. Test coil in dielectric housing to measure winding resistance increase due to eddy currents. Outer diameter of housing is 45.7 cm.

Resistance measurements were made with a HP 4192A low frequency impedance analyzer for a range of frequencies and cross-checked with a second analyzer. Coil resistance values are plotted in Figure 18 as a function of the ratio of the conductor thickness to classical skin depth, δ, a measure of the magnetic field diffusion into a conductor at a given AC frequency, f, where :

$$\delta = \sqrt{\frac{\eta}{f\pi\mu}} \tag{1}$$

η = 1.72 μΩ-cm resistivity of copper, and $\mu = 4\pi \times 10^{-7}$ H/m.

Also plotted in Figure 18 is the ratio of measured AC resistance to the DC resistance. The DC value was calculated to be 45.8 mΩ based on the wire resistivity, length, and crossection. This is in excellent agreement with the low frequency measurement at d_{wire}/δ= 0.25 corresponding to a frequency of 8 Hz.

For the originally planned operating condition for the testbed, the ratio of wire conductor thickness to skin depth in copper for 200 Hz is 1.25. The AC resistance is 4 times the DC resistance and exceeds the original estimate. The electrical-to-mechanical energy conversion efficiency of a full scale design would be reduced significantly unless wire size, construction, or frequency is changed.

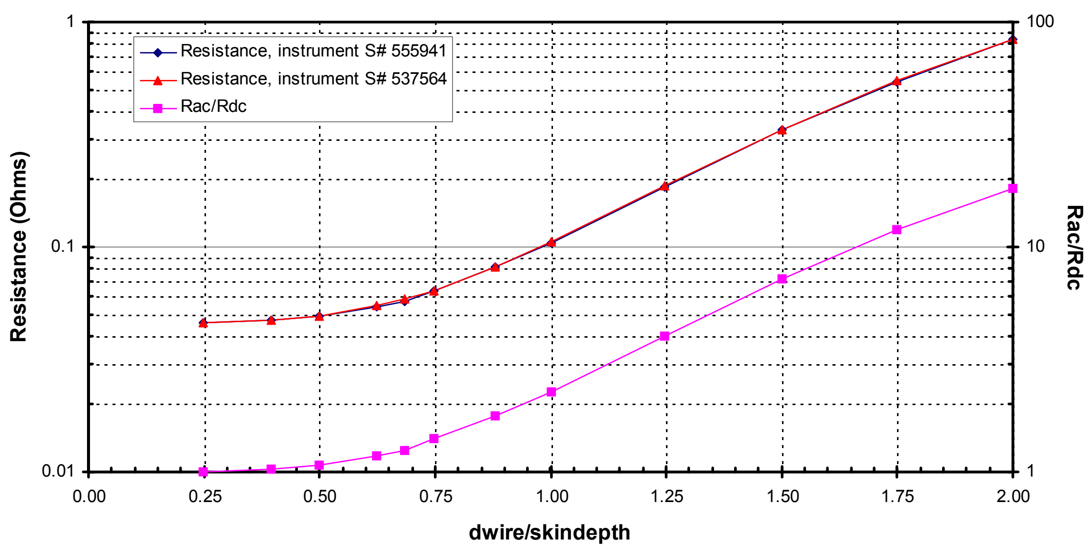

Figure 18. Resistance measurement of test coil as a function of the ratio of wire thickness to skin depth. Wire conductor size is 0.58 cm. Calculated DC resistance of coil is 45.8 mΩ.

Mitigation of Increased AC Resistance

Three options to reduce the AC resistance were considered: using litz wire for the conductor instead of solid wire, reducing the wire size to below a skin depth, and reducing the frequency. The use of litz wire (woven insulated wires formed into a rectangular cable) appropriately sized for the frequency of operation readily mitigates the non-uniform current distributions in solid wire, but the mechanical reinforcement of the cable is problematic without impacting the heat transfer to the coolant. The low modulus of the wire without such reinforcement precludes its use at present, but alternative reinforcement design approaches will be considered in the future.

The use of smaller square or rectangular wire is straight forward, but to maintain coil dimensions and minimize power dissipation, the winding must have more turns. For the same thrust from a motor coil, the voltage must be scaled as the number of turns. This increase must be kept within practical limits for the full-scale motor coil, one of which is the maximum AC voltage that can be typically delivered by a power distribution system for conventional rail. This sets the lower limit for the wire size.

The upper limit for wire size is determined by how large an increase in AC resistance can be tolerated. For an increase of 30%, the measured coil resistance curve suggests the d_{wire}/δ value should be on the order of 0.7 which results in a wire size of 3.3 mm, or #8 AWG.

The change of wire size has a small impact on coil construction and operation. Turns increase from 132 to 380 within virtually the same overall dimensions of winding. The smaller #8 AWG wire with heavy Formar insulation makes 10 turns/layer in 38 layers instead of 6/layer in 22 layers. Coolant channels are the same size, but placed between every other winding layer and capable of removing the same heat from the winding. A fiberglass, B-stage-cured epoxy composite prepreg is wrapped between the alternate winding layers to bond two layers of wire together for axial strength. This is shown in Figure 19. Voltage across the coil increases from 8.3 kVpeak at 150 Hz, which will require only a different transformer step-up ratio. Analysis with the SERTRAIN circuit code indicates that the thrust and lift forces and ohmic heating are virtually identical to previous design that included the ohmic loss design allowance.

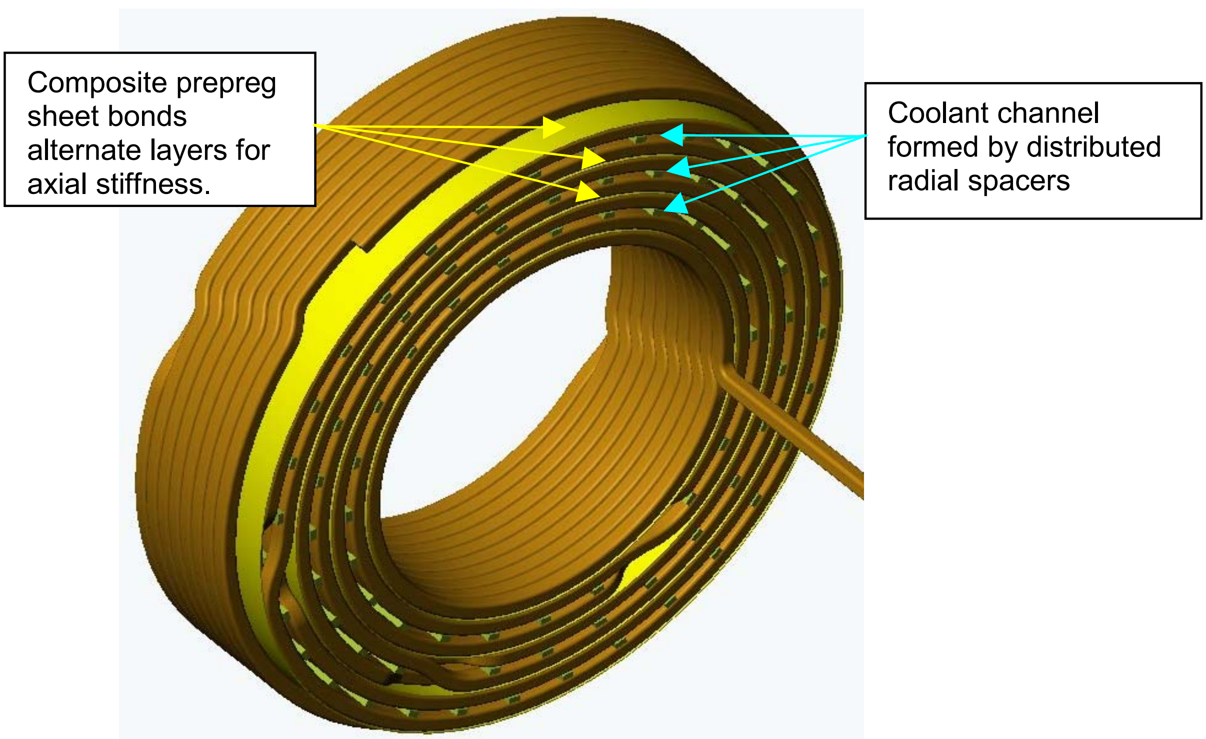

Figure 19. Model of partial winding of SERAPHIM motor testbed coil that shows axial coolant channels placed between alternate layers of winding. Space between layers without coolant is filled with thin fiberglass-epoxy composite prepreg to bond layers.

The new design concept scales directly to the full-scale motor coil described in the earlier sections of this report. Coil OD and height increased by factor of 2 from testbed size, but wire size (#8) remains the same. Turns will be reduced compared to the testbed coil to keep coil voltage less than 27 kVpeak. Four #8 wires are wound in parallel at a time at the same radius in each winding layer, and the four wires are transposed in position midway through the winding of the coil to promote current balance between wires. Analysis with the SERTRAIN circuit code indicates that the modified coil generates the same thrust and lift force, but there is an increase in the heating of the motor coil due to the reduction of winding crossection which requires a slight modification to the cooling system.

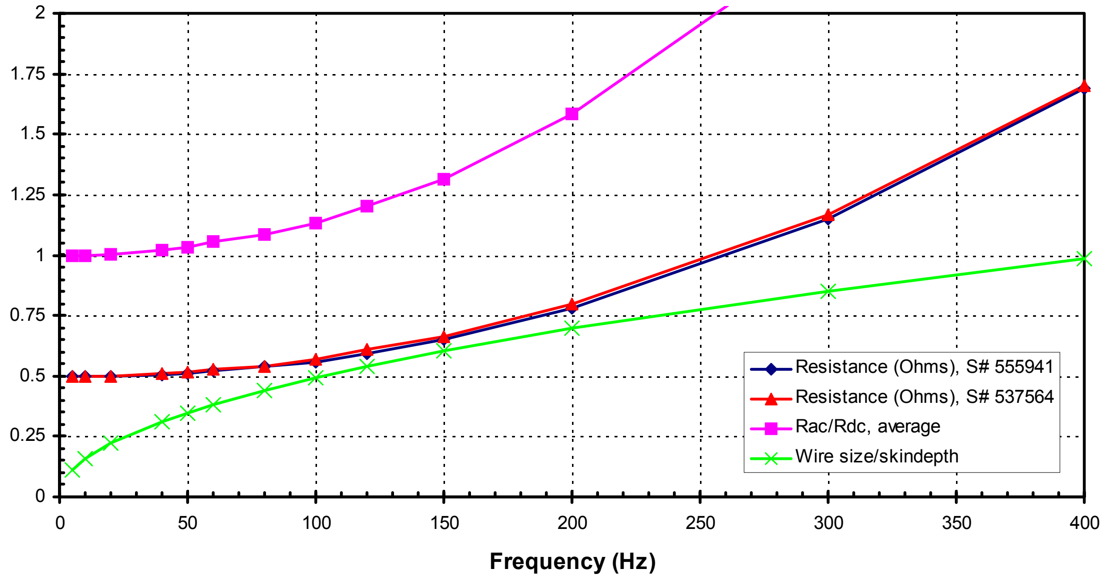

Figure 20. Resistance and resistance ratio of test coil of 380 turns of #8 square copper wire with mock radial gaps for coolant. Wire conductor size is 3.3 mm. Measured DC resistance is 500 mΩ.

Test coils of the #8 square wire as shown in Figure 19 were prepared for confirmation of the loss estimate. The resistance of a 380 turn, 38 layer coil of #8 square wire as a function of frequency is shown in Figure 20. The ratio of wire size to skin depth is also plotted for comparison to the previous chart. For an operation frequency of 200 Hz (wire size/skin depth = 0.7) the AC to DC resistance ratio is 1.6 versus the 1.3 expected from the earlier data, apparently due to the increased number of layers of the coil. To lower the AC to DC resistance ratio to 1.3, the operation frequency will be lowered to 150 Hz. SERTRAIN calculations indicate the full-scale motor can operate at the lower frequency at essentially the same efficiency.

Thermal Design of SERAPHIM Motor

The design of the cooling system presented challenges to maintain the wire temperature at a maximum of 100ºC with constraints of using an oil coolant for its dielectric properties, small coolant gaps for maximum conductor fill, and requiring minimal structure between motor and track coil for maximum magnetic coupling. Analytic thermal models were constructed for the full-scale vehicle and the sub-scale testbed coil designs to evaluate tradeoffs. These models considered fluid flow and heat transfer within the coil winding as well as details and design of the components of the external heat rejection system.

Track coil cooling requirements

It is important to consider the cooling requirements for the track coil. Track coils will be distributed one meter apart along the entire length. The ohmic heating in each coil is proportional to the current squared. Since the current is reduced in the track coils, the instantaneous thermal power is much reduced. Using current design figures, the peak thermal load is 30% that of the peak in the motor coils. Also, the duty factor of the track coils is reduced below the 0.5 design value for the motor coil for two reasons: First, the track coils are spaced closer together than the coils distributed on the car; and second, the track coils only operate when a train is over that portion of the track.

Using current design figures, the maximum heating rate for the track coil is approximately 0.1°K/sec. when a train is above a particular track coil. This results in very little temperature rise even for a long train at low speed.

To estimate the maximum temperature that the track coils can reach after many trains have passed, it is necessary to first determine the average power input into these coils:

$$P = 30kW\left(\frac{4\delta}{Lf}\right)\left(\frac{NL/V}{\tau}\right) \tag{2}$$

where 30 kW represents the maximum power input into the track coil, 4 represents the number of motor coils per car, δ the duty factor of the motor coil, *L* represents the length of each car, *f* represents the track coil per unit length, *N* represents the number of cars in the train, *V* the velocity of the train, and τ the time between trains. With these definitions, the second term represents the duty factor of the track coil while a train is overhead, and the last term represents the fraction of time a train is overhead.

As can be seen from Equation 2, the greatest power input into the track coil occurs at the lowest velocities. Thus the coils near the station will be the most impacted.

The average power from track coil is then equated to the radiative and convective cooling off of the top surface of the coil. No credit is taken for conduction into the guideway structure. The average power radiated and convected is given below:

$$P = \sigma\varepsilon A(T^4 - T_a^4) + hA(T - T_a) \tag{3}$$

where the first term is the radiative power, and the second term is the convective power. *A* is the top area of the coil and T_a is the ambient temperature. The heat transfer coefficient is obtained from Heilman which has been found to be a very good match to experimental data of heat transfer from the earth's surface [14,15].

$$h = 5.383\left(\frac{2}{1.8(T + T_a)}\right)^{0.181}(1.8(T - T_a))^{0.266}\sqrt{1 + 2.857\nu} \tag{4}$$

where ν is the wind velocity and all temperatures are in Kelvin. This correlation is intended for large heated areas (i.e. a parking lot). Heat transfer coefficients are greater for smaller areas. No credit has been taken in this analysis for the fact that the coil area is small, and the wind velocity is assumed zero.

Equating the input power and the convective and radiative power, a surface temperature can be obtained. Using a 20 car train as a worst case, where each car is 25 feet long, a 25 mph velocity, and 60 seconds between trains, a surface temperature of 60°C is obtained. Thus it is assumed, even under these extreme conditions, that no track cooling is required. This assumption requires that the track coil be designed so that conduction to a 60°C top surface is adequate.

Motor Coil Coolant Channel Geometry

Unlike the track coils, the motor coils will require cooling. The SERAPHIM motor is simply a circular coil wrapped on a mandrel. Currently, it is anticipated that the coil will have a 0.83 meter outer diameter, a 0.16 meter inner diameter and a height of 0.065 meters. To maximize the magnetic coupling, it is desired to pack as many amp turns into this volume as possible. Thus, it is desired to minimize the volume dedicated to the cooling system.

Two winding geometries were considered that allowed for inclusion of coolant channels. First, the coils could be wound in pancake layers. In this concept, a layer of wire would be wrapped from the inner diameter to the outer diameter. Then separate layers would be stacked axially to construct the coil. Radial coiling paths would be created by inserting spacers between the layers, allowing the coolant to flow in channels created between the layers and spacers as shown in Figure 21.

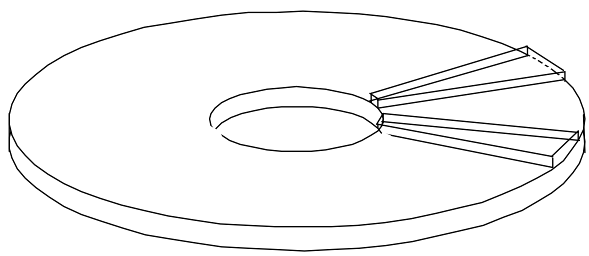

Figure 21. One pancake coil layer with two of many spacers. The coolant flow path is proposed to be radial between the spacers, on the top of the pancake coil shown, and below the next pancake coil that would be mounted above.

This first concept proved to be difficult to manufacture, and also provided a significant challenge to the cooling system design. First, the electrical connections between the various coil layers were difficult to construct, especially at the inner diameter where there is little room. The electrical connections would have to be cooled, and yet, they could not interfere with the coolant flow. Finally, the coolant channels are not of uniform flow area, and thus, the cooling would not be uniform within the coil.

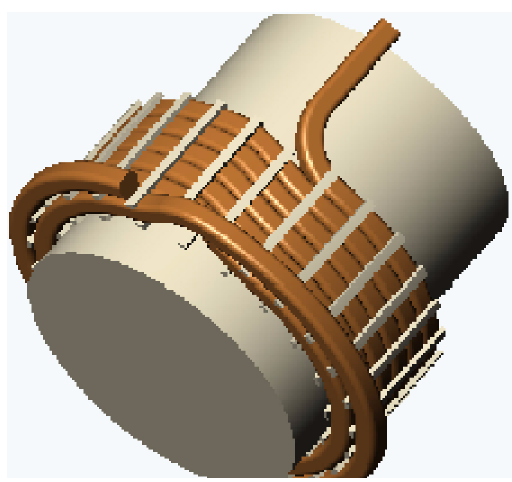

Figure 22. The first radial wire layer upon the mandrel, and the start of the second radial layer. The spacers are placed during the winding process and create axial channels between each wire layer and adjacent spacers.

A second concept was to wind the coil in radial layers instead of axial layers. In this way the spacers would be aligned in the axial direction and the flow paths would be axial as shown in Figure 22. In this concept the electrical connections between the radial layers are created during the winding process. The two coil leads are then brought out through coolant passages so that they can also be cooled.

Cooling Fluid

The coolant has to have a very low electrical conductivity so that it will not result in internal shorts within the coil. Also, the low electrical conductivity will minimize losses that would result from currents induced from the oscillating magnetic field. We have initially chosen Shell Diala oil due to its high electrical resistivity and extensive experience in its use at Sandia. This fluid has a low thermal conductivity and a relatively high viscosity, that makes it less desirable than water as a coolant. However, use of water would require an extensive de-ionization effort to maintain a low electrical conductivity.

Fluid Distribution

One great advantage of the axial coolant channel design is that each coolant channel is identical. This allows for efficient cooling since the waste heat is generated uniformly throughout the coil. However, as will be seen, feeding each channel uniformly is not an easy task. The simplest way to provide uniform flow is to include large coolant plenums above and below the coil. If the plenums are large enough, the flow velocities within each plenum will be low, and each channel will be fed from a constant pressure source and drain to a constant pressure sink. Due to the inevitable tolerance variations in the manufacture of the coil, some channels may be smaller, and receive less flow, and some wire sections may have a slightly higher resistance and generate more heat. However, these variations will be naturally compensated by the decreasing viscosity of the coolant with temperature. This reduction in viscosity will admit more coolant flow to the channels that get the warmest, minimizing differences across the coil.

Unfortunately, we do not have the space available to provide for large coolant plenums. It is desired to keep the electrical gap between the motor and track coils as small as possible to maximize the magnetic coupling. So a large plenum on that side of the coil is not possible. And, it is desired to extract significant forces from the motor coil, so a structure must exist on the opposite side of the coil to support it.

Figure 23 shows conceptually how the coolant is passed through the coil. The flow is supplied to an Axis-symmetric header near the outside radius at the top of the coil (top is defined as the side away from the track coil). This header acts as a manifold to supply flow around the circumference of the coil. From this header, the flow travels radially inward in the outer top plenum. This plenum acts as a manifold to supply flow to half of the axial channels. A divider is placed in the top plenum to prevent flow to the inner half of the axial channels. The flow is collected in the bottom plenum and flows radially inward. The bottom plenum then acts as a manifold to supply flow to the other half of the axial channels. The flow is then collected in the inner portion of the top header, and flows radially inward to be collected by the axisymmetric header near the inner radius.

By splitting the upper plenum in two parts, both the coolant feed and coolant return can be placed near the top. This allows us to minimize the coolant connections at the bottom of the coil. This design also permits better magnetic coupling between the motor and the track coil, and allows for easier cooling of the electrical leads.

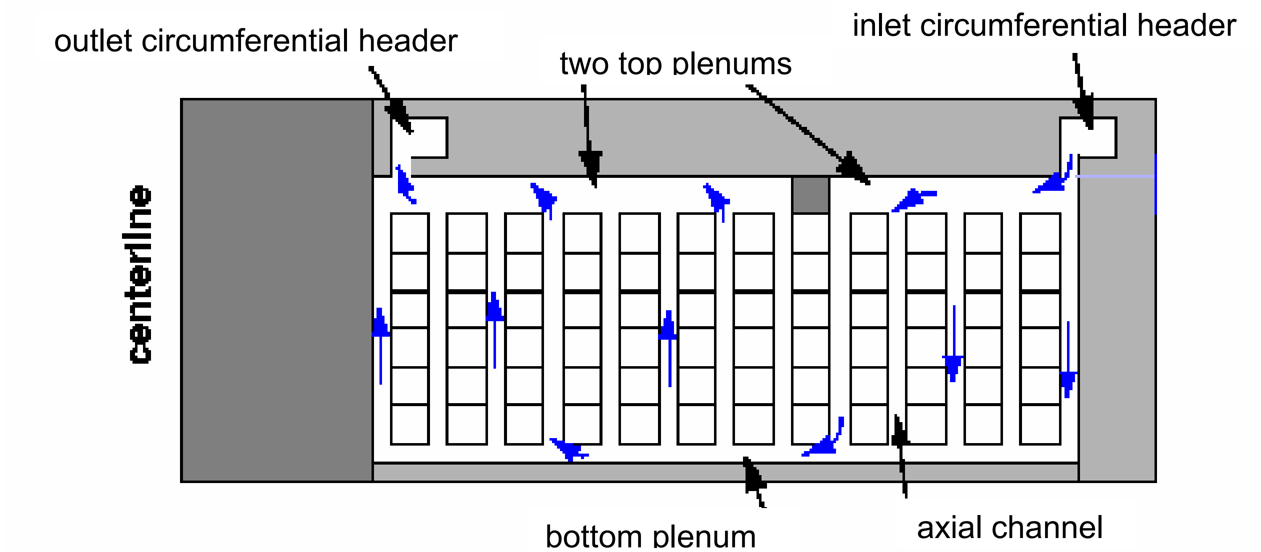

Figure 23. Coolant flow paths through a coil (the number of radial layers and turns per layer are reduced in the diagram for simplicity).

Axial Channel Pressure Drop and Heat Transfer

Prediction of the pressure loss and wire surface temperature is made from empirical relations of laminar flow in the axial channels. These non-dimensional correlations allow prediction of the friction and heat parameters. Then the copper temperature can be obtained by considering the conduction of the waste heat through the insulation layer. Scaling analysis shows that the copper temperature does not vary significantly as a function of radial position within the wire (or shielding behind a spacer) due to the high thermal conductivity of the copper. It is also determined that if any single axial coolant channel is blocked, the heat can be easily conducted along the copper wire to nearby coolant channels.

These empirical results can be summarized here. There is a 8°C rise of the coolant as it passes through the motor coil at the design flow rate of 60 gal/min. A temperature drop of 12°C occurs between the coolant and the wire surface. A temperature drop of 3°C occurs through the wire insulation. Thus, if the coolant is supplied at 45°C, the maximum copper temperature is 68°C. These results were conservatively calculated assuming a 50% duty factor while the train was operating at the condition of maximum thermal waste power. In actual operation, the train would never be continuously operated at this condition.

The above estimates of the coil temperature assume that the fluid is fed evenly to each of the axial channels. As will be shown below, the flow is not uniform. So the total flow will be increased so all channels receive adequate flow.

Coolant Flow: Plenum Geometry

A waffle-iron plate geometry is used to construct the top and bottom plenums. This geometry allows for fluid flow between the mesas. The high spots of the waffle plate are approximately the same physical size as the wire width. At this point it has not been determined if the high spots of the waffle plate are square mesas that are created after a series of perpendicular cuts with a mill are performed, or round mesas. The round high spots would be made by gluing down short sections of rod to a flat plate. Figure 24 shows a conceptual design for the lower plenum using round mesas. The upper plenum is similar, but includes a divider that separates the plenum into inner and outer portions as shown in Figure 23.

The round mesas have a few advantages. Since they are individually placed, they can be placed to mate well with the wire coils. Also, their round cross-section would provide less resistance to the radial flow of coolant in the passages between the mesas. Third, the fabric reinforcement cloth within the mesas will be cut less than if square mesas were used. Whenever a fabric reinforced composite is cut, the strength is reduced and material may be lost near sharp corners.

The flow resistance of the waffle plate is of great interest since it is desired to provide equal coolant flow to each axial channel. If some channels receive more flow due to an uneven distribution, then the total coolant flow has to be increased to maintain the desired minimum flow to each channel.

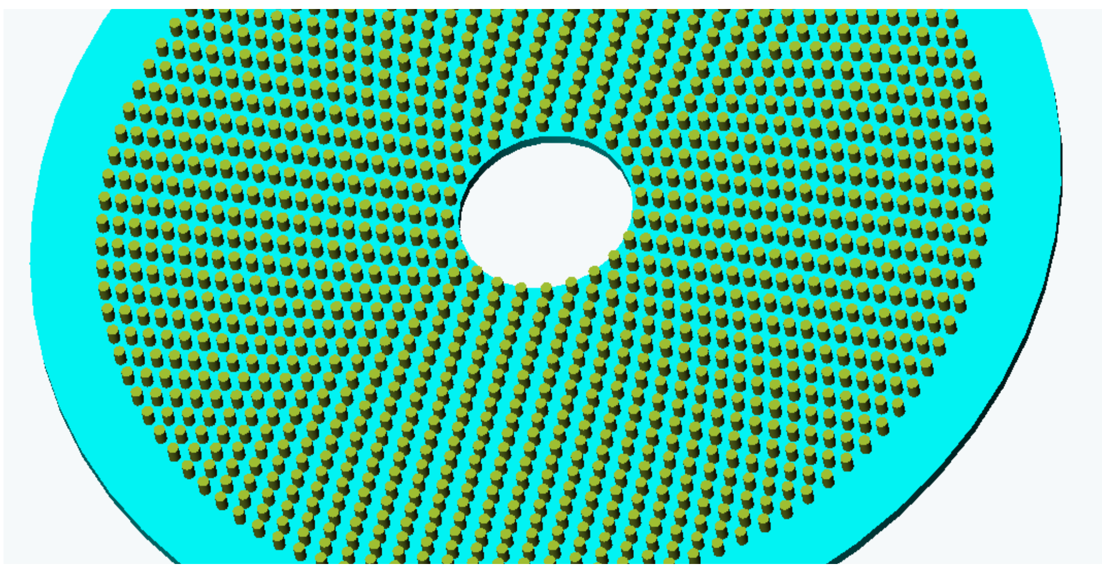

Figure 24. Lower coolant plenum geometry using round mesas. Each ring of mesas aligns with a layer of wire in the coil.

A fluid flow model was constructed to simulate the radial flow through the waffle plate plenums. The model considers the geometry created by the outer portion of the upper and lower plenums and the axial channels that connect these two plenums. It is assumed that the fluid is distributed uniformly around the outer diameter of the top plenum and removed uniformly at the dividing diameter (at the radial location of the separator in the upper plenum) of the lower plenum. The same model can be used to model the flow inside of the dividing diameter simply modification of the input geometry parameters.

Due to the segmented nature of the coil, the pressure distribution in the plenums is divided into segments equal to the radial wire spacing. At each segment end, fluid is extracted through a specified number of axial channels and is added to the flow in the lower plenum. The following equation presents the momentum balance for the radial flow within the two plenums:

$$P_{-} - P_{i+1} = \frac{f\Delta r}{D}\frac{\rho V_i^2}{2} + \rho\left(\frac{r_i}{r_{i+1}}V_i^2 - V_{i+1}^2\right) \tag{5}$$

where the subscript i represents the radial location, r is the radius, V is the velocity, ρ is the fluid density, D is the hydraulic diameter, f is the friction factor and P is the static pressure. It turns out that the last term in the above equation is very important since the pressure changes due to the acceleration of the fluid is significant.

A mass balance relates the flow in the axial channels and the radial plenums:

$$AN_iU_i = \left(V_{i+1} - \frac{r_i}{r_{i+1}}V_i\right)2\pi(1-\alpha)hr_{i+1} \tag{6}$$

where U is the axial velocity in the *ith* layer of axial channels, A is the axial channel cross-sectional area, N is the number of axial channels in layer i, h is the plenum height and α is the fill fraction of the plenums (fraction occupied by structure).

To complete the equation set, a momentum balance for the axial channels is required:

$$P_{Ti} - P_{Bi} = \frac{fL}{D}\frac{\rho U_i^2}{2} + k\frac{\rho U_i^2}{2} \tag{7}$$

Here, k represents the entrance and exit pressure losses in the axial channels, and L represents the axial channel length. The friction factor and hydraulic diameter in Equation 7 are evaluated for the axial channel conditions, and therefore typically not the same numerical value as used in Equation 5. Unlike Equations 5 and 6, the top and bottom plenum pressures are explicitly labeled in Equation 7.

Equation 5 requires an initial pressure and velocity for each plenum. Since the fluid is assumed to be incompressible, the solution is independent of the pressure level. So the incoming pressure at the upper plenum is assigned a zero value and the velocity is set so that the design flow is realized. The radial velocity in the lower plenum at the outer radius is set to zero. The pressure in the lower plenum at the outer radius is assigned a representative value, and the equations are integrated to the divider diameter. The total flow through the axial channels is determined and checked against the design value. If they are not equal, the pressure boundary condition in the lower plenum is adjusted accordingly. With an iterative process, the proper pressure boundary condition is determined and the solution is accepted.

Figure 25 shows the pressure distribution in the two plenums for typical values for the flow and geometric parameters.

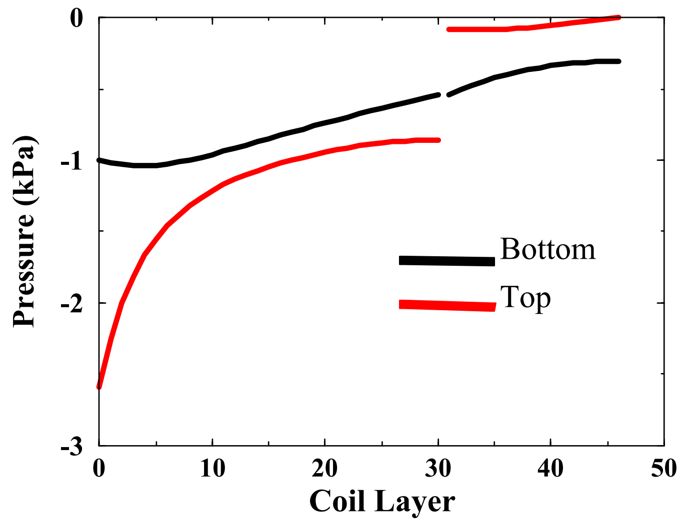

Figure 25. Pressure distribution in the top and bottom plenums. The break in the plot is the dividing radius. The pressure in the top plenum is not continuous at the dividing radius.

The results shown in Figure 25 indicate that the axial channels near the inner most coil layers are subjected to the largest pressure gradient and therefore the greatest flow. This is where the radial flow in the upper plenum is the largest, resulting is a locally low static pressure. Fortunately, there are few channels near the inner radius of the coil, so most of the channels do not get this increased flow. Visually, it is obvious that most of the channels experience nearly identical flows since they all experience nearly identical pressure differences. Figure 26 shows the distribution of the flow through the axial channels as a function of radius. By moving the dividing radius closer to the inner mandrel, it is possible to get even more uniform flow. First, it will lower the flows in the outer layer since it will increase the number of axial channels in that layer, and conversely raise the flows in the inner layer. Second, the acceleration of the upper plenum of the inner layer is less due to the smaller ratio of the inner and outer radii in that section.

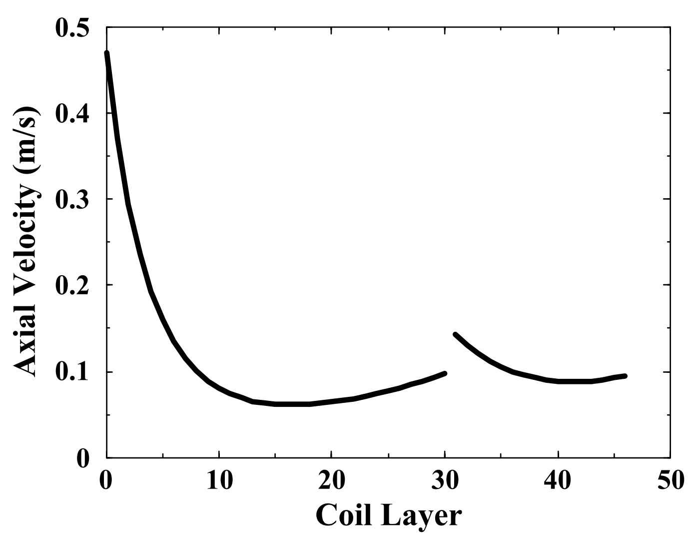

Figure 26. Axial velocity distribution in the axial channels. The break in the plot is the dividing radius.

The results presented in Figure 26 suggests that the channels near coil layer 15 might heat up the most since they receive the least flow. However, the flow through these channels is not significantly less than the majority of the other channels.

Coolant Flow: Circumferential header geometry

In the previous section, the flow was assumed to be radial in the plenums. That assumption is dependent upon the axisymmetric headers in Figure 23 being sized large enough so that the entire circumferential perimeter of the top plenum is fed uniformly. To accomplish this, the pressure variations in this circumferential channel must be small compared to the pressure losses in flowing through the plenums and axial channels. It was determined that to maintain a nearly constant pressure in this circumferential channel, the channel had to either be very large, or fed at a number of locations.

If this channel is fed in only one location, the maximum distance the fluid must travel is one half the circumference, and the fluid volume that travels in each direction away from the feed is half the total flow. This is easily generalized to N feed locations, where the fluid velocity in the circumferential header is given below:

$$V(\theta) = \frac{F}{2AN}\left(\frac{\pi - N\theta}{\pi}\right) \tag{8}$$

where F is the total volumetric flow, A is the circumferential header cross-sectional area, and θ is the angular distance the fluid has traveled. The static pressure at any angular location can be found by integrating the following equation:

$$P = \int_0^\theta f \frac{\rho V^2}{2} R d\theta + \rho \frac{V^2(0)}{2} - \rho \frac{V^2(\theta)}{2} \tag{9}$$

Figure 27 shows the pressure distribution obtained along the circumferential header when four feeds are used. In this case, the fluid only has to travel a maximum of 45 degrees from each feed location. It is seen here that the acceleration term dominates over the frictional term, and the static pressure increase along the flow path. This increase is not negligible when compared to the pressure changes identified in Figure 25. So one might expect that the locations away from the feeds will get greater flow. To counter this condition, the feeds could be aligned radially so the incoming momentum would aid the incoming flow (the analysis does not account for any incoming momentum). Also, Figure 24 shows a pattern in the mesa alignments. Radial flow is easier from some circumferential positions due to the alignment of the mesas. It is possible that the orientation of the plenum pattern could be used to offset the non-uniform feed suggested by Figure 27.

The pressure distribution depicted in Figure 27 is obtained assuming that the fluid enters equally at all circumferential locations. However, since the pressure is greatest at 45 degrees, more fluid will enter at this position.

This section reveals that the flow acceleration terms are dominant when compared to the frictional losses. Thus, the local flow rates are a stronger function of the velocities in the circumferential header than the distance from the manifold feed. The distribution from the circumferential headers has proven to be a larger problem than the distribution from the radial plenums to the axial channels.

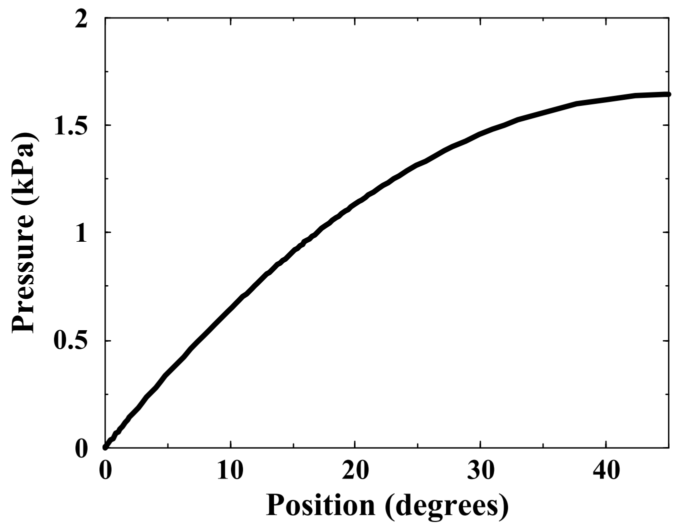

Figure 27. Pressure distribution along a circumferential header for four feeds.

One way to avoid this poor distribution from the circumferential header is to require the fluid velocities in the radial plenum to be significantly higher than the velocities in the circumferential header. This can be accomplished in one of three ways.

First, the radial plenum can be made significantly smaller. This is not desirable since this would increase the pressure required to pass coolant through the motor.

A second method is to include flow orifices at the exit points from the circumferential header so that the pressure drop is dominated by these orifices with high velocities. This would also increase the pressure drop through the motor and an increase the complexity of the assembly.

The third method is to decrease the velocity in the circumferential header. However, calculations have shown that large increases are required, and there is little room for this and still retain structural integrity. An alternate method to make the circumferential header of variable size. Thus, as the volumetric flow rate decreases in the direction of flow, the fluid velocity remains constant. This may prove to be the best solution to maintain uniform flow in the motor.

Conclusions from Thermal Design

This study presents the heat transfer and coolant flow design for the SERAPHIM motor. The heat transfer has been shown to be adequate for both the motor coils and the passively cooled track coils. The most difficult aspect of the design is the assurance of nearly uniform flow through the 5600 axial channels. Flow distribution via the circumferential header is not uniform due to the increasing pressure as the fluid decellerates. This results in greater flows between the fluid inlets than near the fluid inlets.

Modeling and Stress Analysis of SERAPHIM Static Testbed Coils

SERAPHIM motor coil design options

Initially, a radial cooled flow concept as shown in Figure 28 was studied and evaluated. This concept required 25 psi hydraulic cooling pressures, use of higher-temperature, more costly, G-11 dielectric housing material for elevated temperature operation (130°C), and very good interface bonding between coil wires and cooling spacers. Complex manufacturing problems were identified along with high thermal stress levels at horizontal cooling spacer bonding locations; therefore, this concept was abandoned for an axial cooled design concept.

The axial cooled concept, already shown in Figure 16, incorporates a more easily manufactured system and better heat transfer resulting in a lower hydraulic pressure head loss. Electromagnetic forces remain unchanged with either cooling concept, but the later offers reduced thermal and hydraulic stresses. This configuration employs use of a more common G-10 housing material [16].

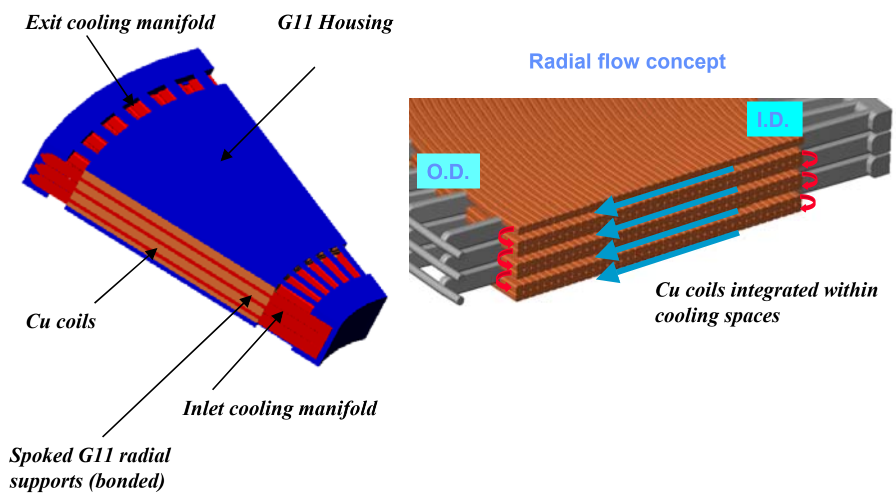

Figure 28. Initial coil concept that used coolant flow in the radial direction between stacked, pancake-type winding layers.

SERAPHIM testbed coil modeling

A detailed solid model is shown in Figure 29 of a half scale SERAPHIM axial cooled motor coil that was created using SolidWorks [17]. For meshing purposes, this geometry was simplified using accepted design to analysis techniques to remove small problematic features such as fillets, chamfers, gaps and interferences. Care was taken to ensure the physical aspects were captured adequately. For example, all spacers are bonded to the wire insulation, and thus were meshed contiguously to the wire. There are approximately 2600 spacers distributed non-uniformly in this configuration. The solid model was then exported via STEP format and meshed using Patran [18]. The mesh was then exported into an Exodus format for structural finite element analysis in JAS3D [19,20]. This process was repeated through iteration as the design concept was developed.

For normal SERAPHIM motor coil operation, load and geometric symmetries exist, therefore only one half the coil geometry was needed. The model contains approximately 469,000 hexahedral elements and nine material blocks, although there are about 1300 individual pieces that are included, mostly spacers placed at irregular intervals forming constant area cooling channels. Care was taken to ensure element aspect ratios of 4-to-1 or better in the high stress areas.

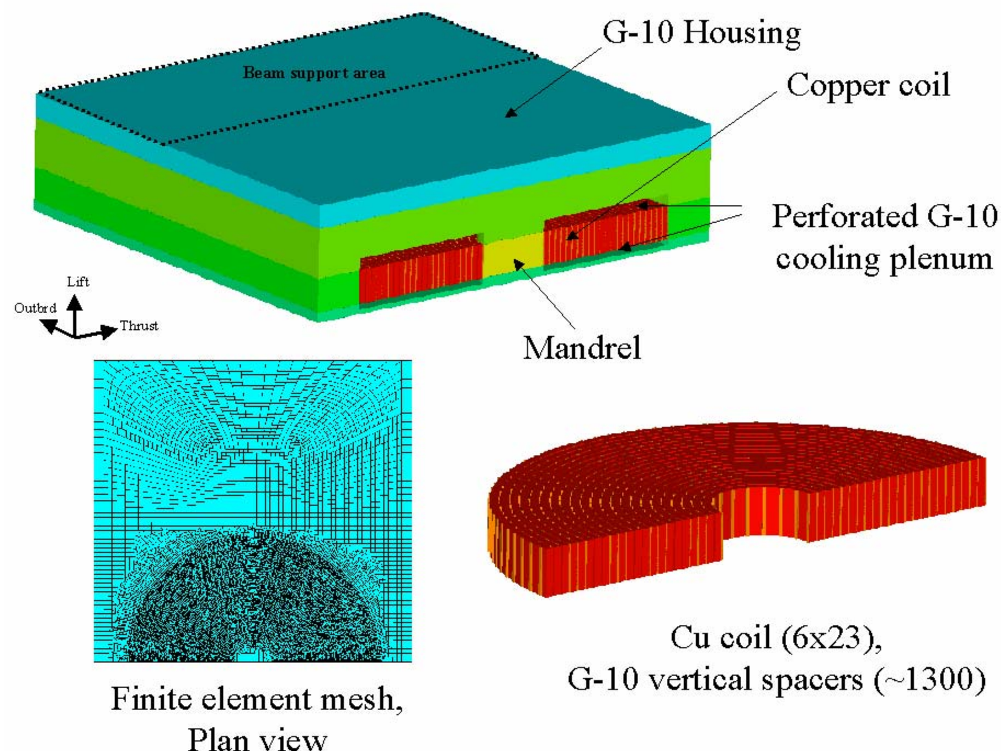

Figure 29. Finite element model of axial cooled motor coil.

Electro-magnetic (EM), thermal and hydraulic loads were quantified and applied as driving boundary conditions. A fixed displacement boundary at the beam support location was used as shown in Figure 29. A symmetric displacement boundary was also applied at the centerline of symmetry as only a half coil section was modeled. A cooling fluid temperature boundary condition was applied to the SERAPHIM motor coil materials for thermal stress computations. The maximum pressure head for cooling is estimated at 10 psi. This boundary condition was applied to all (~1300) interior cooling channels within the model.

EM Lorentz force density distributions were calculated from solutions of vector potential using the currents determined by the SERTRAIN circuit simulation code, and mapped on to the model using Atheta2exo [3,21]. This analysis process is shown schematically in Figure 30.

Coil configurations were considered where the center of the track coil was aligned or offset to the motor coil. The offset case contains lift, thrust and transverse components while the aligned case produces zero thrust but high lift. Results presented here are for a motor coil offset 5.2 cm from the track coil, which is a position of peak thrust and significant lift. In operation, the SERAPHIM motor coil moves over a track coil at varying speeds as the train accelerates. The Lorentz force distribution within the motor coil changes as it moves relative to the track coil.

The 5.2 cm static offset case is considered to be a realistic design point for the static test bed apparatus because it contains significant force contributions in all directions. For this case the static peak thrust and lift component sums are 6.6 kN and 18.4 kN, respectively. Symmetric transverse forces also exist and are included in the analysis.

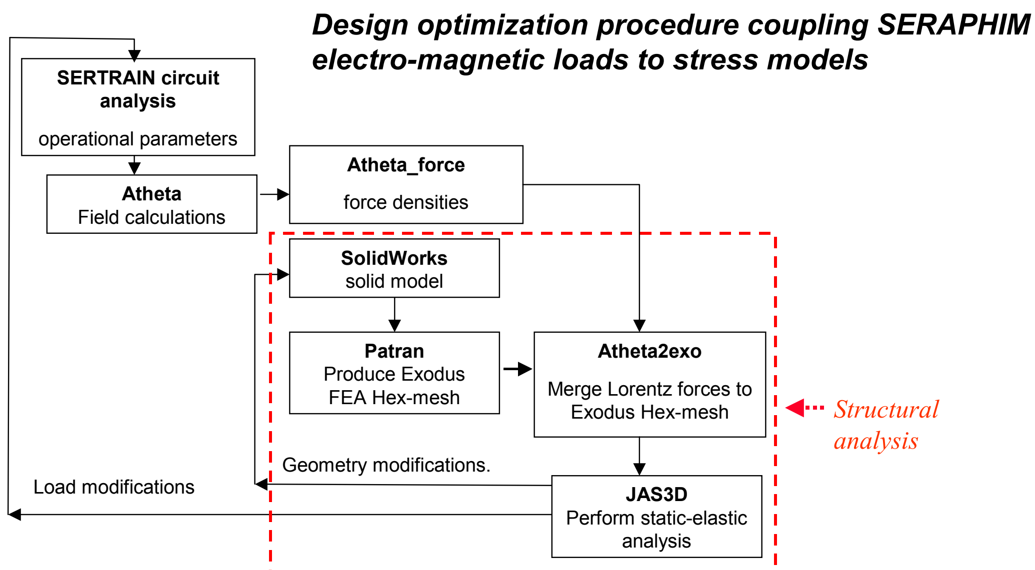

Figure 30. Analysis process for merging Lorentz forces to an Exodus finite element model.

Table 6 lists the material property specifications used for this analysis. Static linear elasticity was assumed. The directional property variations are small, however the thermal strain rates of the G-10 change with fiber orientations and were included in the analysis.

Table 6. Material Property Specifications for the Analysis of the Axial Cooled SERAPHIM Motor Testbed

Component	Material	Expansion coefficient (ppm/°C)			Modulus (Msi)	Temperature (°C)
		X, thrust	Y, transverse	Z, lift		
Wire	Copper	16.97	16.97	16.97	6.5	100
Mandrel and housing	NEMA G-10 laminate	13	13	65	1.9 0.38 plenums	23-49
Winding spacers	NEMA G-10 laminate	65	65	13	1.9	100

Stress Analysis Results

A static stress analysis of the SERAPHIM axial cooled motor coil was performed for a 5.2 cm offset case. This section lists case results obtained for key locations with emphasis on the interfacial bonding between the G-10 and the coil at the lower plenum plane location. Five cases were examined as summarized in Table 7.

Cases 1 through 3 show independent results for pressure, EM and thermal loads, respectively. Cases 4 and 5 show results of combined loads. In all cases, identical material properties and temperature increases were assumed excepting Case 5 calculations. In this particular simulation, the modulus of the G-10 above and below the coil was scaled to 20% of its nominal value to account for the cooling manifold (see Figure 29). The cooling manifold is constructed by machining away 80% of the solid, thereby, producing a less stiff material. Also in Case 5, a cooling fluid temperature of 49°C was used for housing materials and 100°C for the wire. These values are more realistic for steady state operation of the testbed apparatus.

Case1 assumes a 10-psig pressure loading only. The internal pressure acts on ~1300 cooling channels and produces small material stresses and deflections. The maximum overall deflection of the motor coil is $13x10^{-6}$ inches toward the track coil. Although this load is small, it is used in the combination load cases.

Case 2 shows the structural response of the motor coil due to EM forces alone. In general, the material stresses and deflections are also low. The peak overall static deflection away from the track coil is $1.7x10^{-3}$ inches away from the track coil.

Case 3, the thermal component, produces the dominant material stress, although the pressure and EM loads also contribute. For this pure thermal loading case, the peak calculated overall deflection is $41x10^{-3}$ inches toward the track coil. The bonding shear stress of the lower coolant plenum to the bottom of the winding is nominally 400 psi and the bonding tension is 750 psi with peaks of 2500 psi at the inner and outer edges of the coil. Figure 31 and Figure 32 show these distributions.

Case 4 shows the results for the combined loads of pressure, EM and temperature. A conservative operational temperature increase from 23 to 100°C was assumed for all motor coil components. The peak calculated deflection is $37x10^{-3}$ inches toward the track coil at the mandrel location. Most of this deflection is due to thermal loading, although EM and pressure also contribute. The bonding shear stress is nominally 250 psi and the tensile bonding stress is 500 psi with peaks occurring in localized locations around the inner and outer diameters of the coil (see Figure 33 and Figure 34). The wire strain is 0.18% and the wire stresses are between 3 and 8 ksi. The G-10 housing stresses are within 8 ksi and the spacer stresses are all within 13.4 ksi. The vertical shear bonding stress is nominally 0.4 ksi with maximums of 5.8 ksi at inner and outer coil diameters.

Table 7. Stress Results Summary for Cases 1 Through 5.

Case No. Load type	**1 Pressure**	**2 EM**	**3 Thermal stress**	**4 Pres/EM/thermal**	**5 Pres/EM/thermal**
Thermal expansion type	none	none	isotropic	orthotropic	orthotropic
Material assumptions	Table 6	Table 6	Table 6	Table 6	Table 6, 20% G-10 @ manifold loc.
EM force (kN)	0	Thrust=6.6 Lift=18.4	0	Thrust=6.6 Lift=18.4	Thrust=6.6 Lift=18.4
Temperature (°C)	23	23	23-100	23-100	Wire, 23-100 G-10, 23-49
Pressure (psig)	10	0	0	10	10
"Z" deflection (in)	$-13x10^{-6}$	$1.7x10^{-3}$	$-41x10^{-3}$	$-37x10^{-3}$	$-16x10^{-3}$
Bonding shear stress (psi)	3.9	34	400, (Fig. 30)	250, (Fig. 32)	50 average 150 max, (Fig 34)
Bonding tensile stress (psi)	4.5	149	750 average 2500 max, (Fig 31)	500 average 3000 max, (Fig 33)	200 average 250 max (Fig 35)
Wire V-Mises stress (psi)	26	432	4000 average 8000 max	3000 average 8000 max	4000 average 9500 max
Wire strain (in/in)	$3x10^{-6}$	$6x10^{-5}$	0.0017	0.0018	0.0014
G-10 V-Mises stress (psi)	14	257	9000	8000	4540
Spacer V-Mises stress (psi)	x	x	x	13400	7000
Spacer shear stress (psi)	x	x	x	5800	1390

In Case 5, an attempt was made to understand how lowering the effective modulus of the G-10 (cooling manifold) located above and below the coil would impact bonding of the coil to the G-10. The modulus of the G-10 in these areas was reduced by 80% to account for a loss of volume that would be machined away to form the cooling manifolds. This representation is believed to represent the most realistic of the study. Case 5 also addresses more realistic steady state temperature distributions within the motor coil as well as modeling of the more compliant waffle-patterned manifolds above and below the winding. In this combined loading case, pressure, EM, and thermal loads were applied simultaneously as in Case 4.

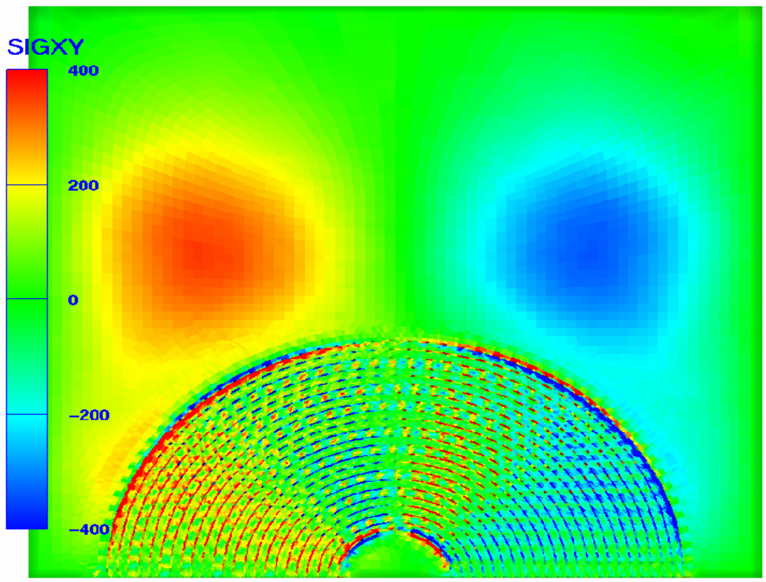

Figure 31. Bonding shear stress (psi) distribution of the lower coolant plenum to the bottom of the winding for a pure thermal load case (Case 3, Table 7).

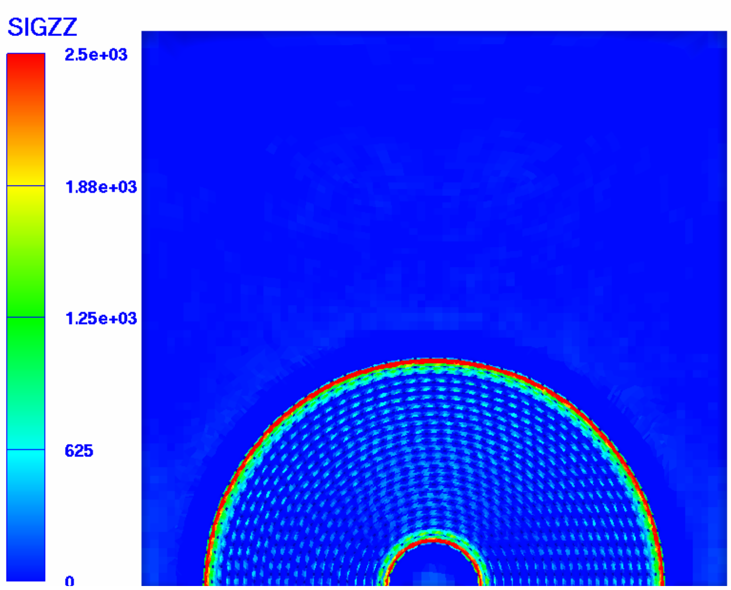

Figure 32. Bonding tension stress (psi) distribution of the lower coolant plenum to the bottom of the winding for a pure thermal load case (Case 3, Table 7).

The peak overall deflection is reduced to $16x10^{-3}$ inches toward the track coil at the mandrel location. The bonding shear and tension is reduced to 150 and 200 psi, respectively. Figure 35 shows the shear stress distribution plotted with two different maximum contour levels. Figure 36 shows the bonding tensile stress distribution for this case.

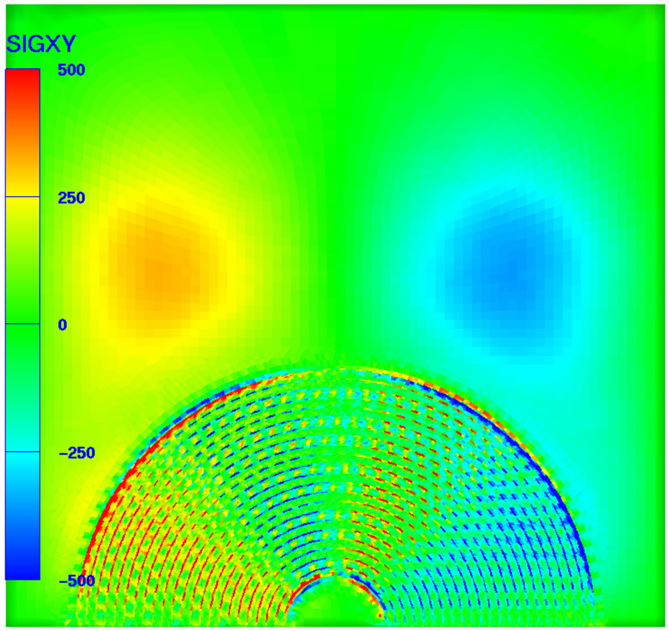

Figure 33. Bonding shear stress (psi) distribution of the lower coolant plenum to the bottom of the winding for combined loads (Case 4, Table 7).

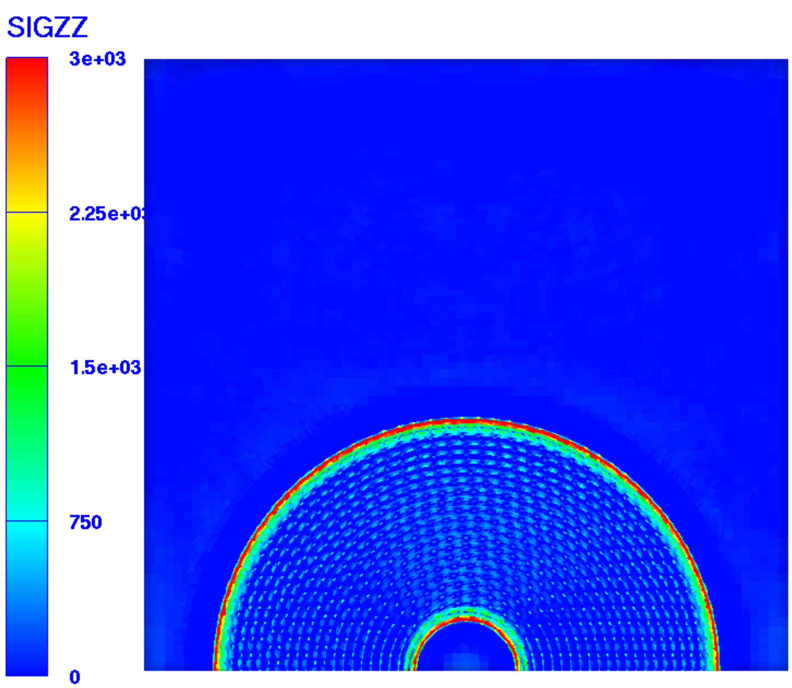

Figure 34. Bonding tension stress (psi) distribution of the lower coolant plenum to the bottom of the winding for combined loads (Case 4, Table 7).

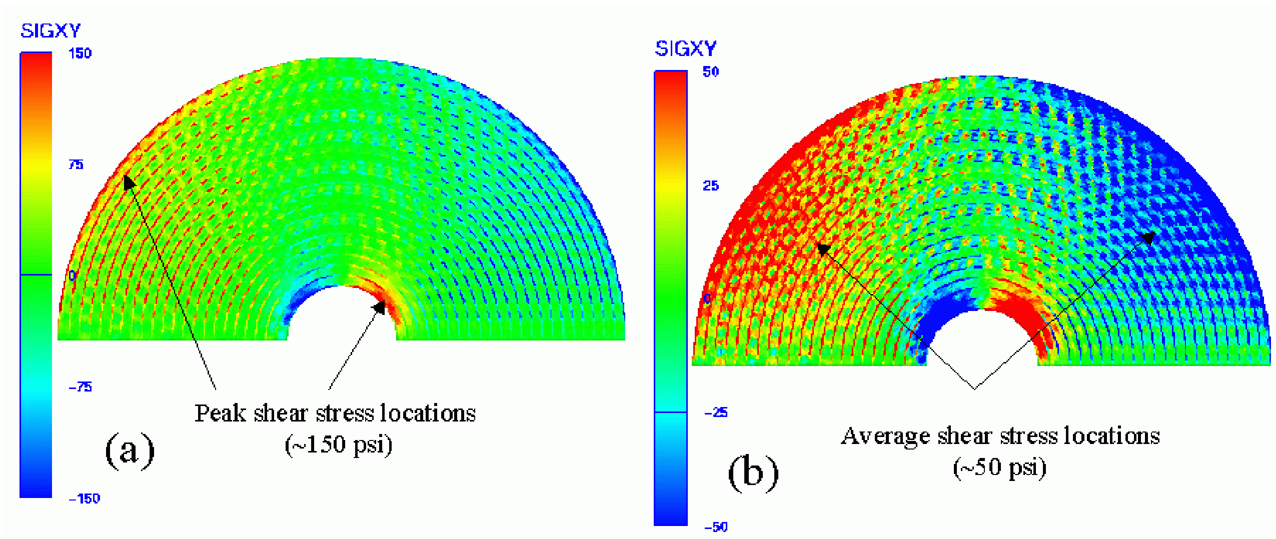

Figure 35. Bonding shear stress (psi) distribution of the lower coolant plenum to the bottom of the winding for combined loads (Case 5 in Table 7). Plots *a* and *b* use different maximum contour levels to show details.

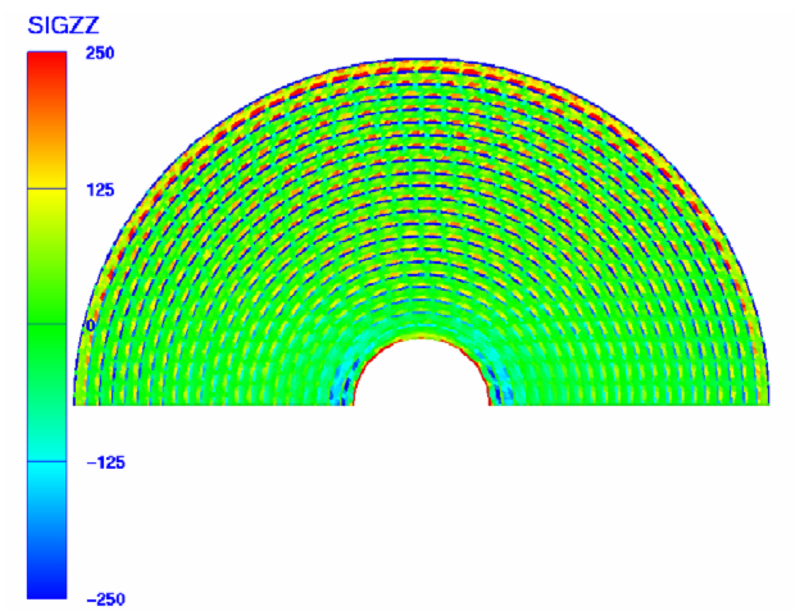

Figure 36. Bonding tension stress (psi) distribution of the lower coolant plenum to the bottom of the winding for combined loads (Case 5, in Table 7).

Table 8. Dynamic Load Estimates for 300 Hz Mechanical Vibration.

Weight of motor coil, (lb)	170
Mass of motor coil, (lb-s^2/in)	0.44
Lifting load, (lb)	4000
Peak EM deflection (Case 2), (in)	1.7x10^{-3}
Equivalent SDOF stiffness, (lb/in)	2.37x10^6
Equivalent SDOF natural frequency (Hz)	369
Driving frequency (Hz)	300
Frequency ratio, ($f/f_{natural}$)	0.81
Dynamic load factor	4.0
Estimated peak deflection due to EM, away from track, (in)	6.8x10^{-3}
Total estimated combined deflection toward track, (in)	-10.9x10^{-3}

The SERAPHIM motor coil is also subject to dynamic vibration in addition to EM, pressure and thermal loads. A 300 Hz input harmonic excitation is induced by 150 Hz AC current oscillations within the conductor wires. This vibration increases the stresses and deflections of the system through a transmissibility function [22]. This increase in load level is known as a dynamic load factor (DLF). Table 8 lists these results. As shown, a DLF of 4.0 exists. This amplifies the EM induced stresses. Thermal and pressure loads are not affected.

In the modeling and analysis effort, the wire cross section was assumed to be rectangular which significantly simplified the finite element model. But, the section actually has rounded corners. This simplification, along with the space allocated for radial coolant flow in the plenums, underestimates the amount of wire contact area that is bondable to the lower manifold by a factor of five. Therefore, the calculated bonding shears and tensions listed in the results summary (Table 7) are too low and must be increased to account for this reduction in area.

Table 9 lists the best estimates of the SERAPHIM motor coil response maximums for components critical to successful operation of the SERAPHIM test bed. These values include the loading conditions of pressure, EM, temperature, vibration, and reduced wire contact area. Minimum material allowable limits are given and corresponding safety margins are calculated. As shown, motor coil deflections are well within the gap tolerance that separates it from the track coil, wire strains are small and stress safety margins vary from 2.9 to 7.8.

Table 9. Best Estimates of SERAPHIM Motor Coil Response Maximums Including Pressure, EM, Temperature, Vibration, and Wire Contact Area.

Response Type	Calculated value	Material allowable	Safety margin
Motor coil deflection toward track, (in)	-10.9x10^{-3}	.125 air gap	.114 Clearance
Wire strain, %	0.16	30 [Ref 23]	189
Coil-housing bonding shear stress, psi	760	2260 [Ref 24]	2.9
Wire Von Mises stress, psi	9500	37000 [Ref 23]	3.9
Housing Von Mises stress, psi	4500	35000 [Ref 16]	7.8
Spacers Von Mises stress, psi	7000	35000 [Ref 16]	5.0

PLANNED TESTING

Testing of sub-scale coils will be in a static testbed shown in Figure 37 in a configuration similar to the geometry shown in Figure 1. The coils will be electrically driven by the circuit shown in Figure 38. Since the coil testing is static, a passive, shorted motor coil with coolant will be used for the track coil. Total losses will be quantified that include the influence of the cooling system and structural components. Lift and thrust forces will be measured for a range of coil positions and clearance gaps. This data, along with electrical diagnostics will provide benchmarks for comparison to our circuit simulation codes based on a coil design that is scalable to a range of applications.

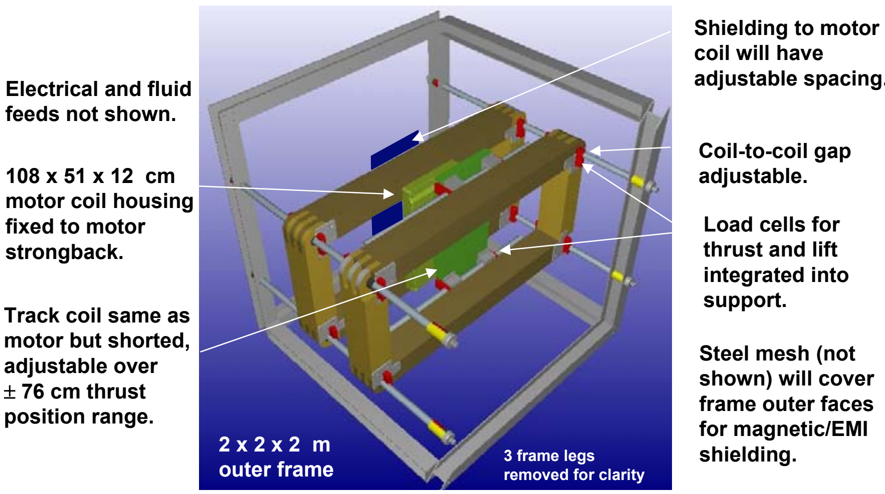

Figure 37. Static testbed frame holds coils with their axis of symmetry in the horizontal plane. Relative positions of coils are variable.

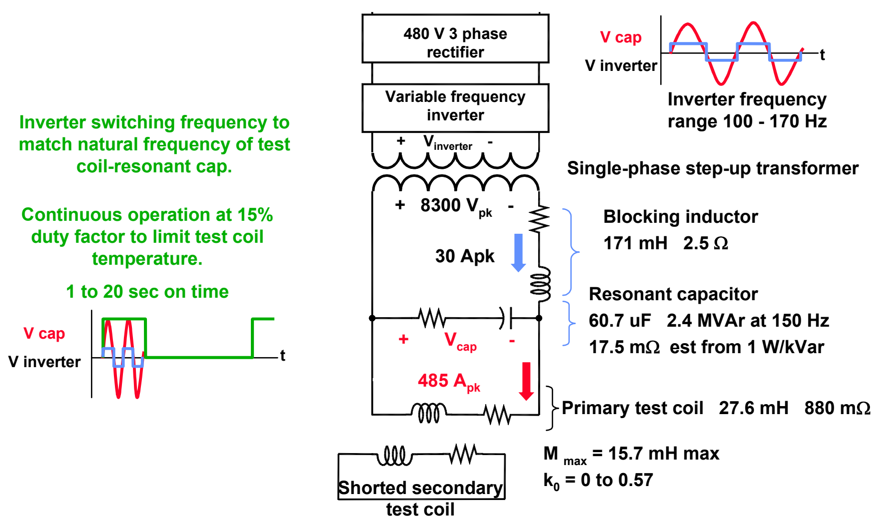

Figure 38. Power supply circuit to drive the motor coil for the static testbed.

The mechanical and thermal response of the coil will also be compared to design calculations. Fiber-optical strain and temperature gauges are integrated into the coil winding. Mechanical response of the coil housing will be monitored with optical and physical displacement gauges. Infrared imaging will be used to evaluate the winding temperature distribution from the bottom surface of the housing. Long-duration, high-power testing is planned to evaluate coil reliability and life.

Final design of the static coil testbed is complete and fabrication of system components that includes coils, power supply, and cooling and control systems is in progress. Assembly will be complete in the second quarter of 2002, followed by testing.

Fabrication of coils for the testbed is nearing completion. A coil winding with its fiber optic temperature and strain gauges is shown in the lower half of its housing in Figure 39. Working with Stangenes Industries, Inc., a fabrication process was developed to readily and accurately wind the coil with the numerous spacers for coolant flow.

Measurements of the inductance and resistance of these coils is in good agreement (<6%) with values determined during final design using pre-fabrication tests. Additional diagnostic tests such as mutual inductance, mutual inductance gradient, and coolant flow balance are planned prior to testing with the inverter. Thrust and lift will be measured over a range of coil positions at increasing power levels. Following quantification of losses, the coils will be tested for long duration (days to weeks) and coil deformation monitored to identify lifetime issues. Finally, magnetic shielding options will be investigated to determine tradeoff between additional mass, coupled losses, and field reduction.

Figure 39. Winding of sub-scale coil for the static testbed in the lower half of the housing body. Cables for fiber optic temperature and strain gauges are wrapped on coil mandrel.

FUTURE DEVELOPMENT

Additional work is recommended to follow the design effort of this project to establish the technical and economic viability of the SERAPHIM motor. The static testing outlined in the previous section will verify the thrust force developed by the motor, the AC losses and the integrity of the mechanical construction and cooling methodology. Given this design is rooted in performance requirements for a transit application, this testing is a necessary step to demonstrate functionality. However, additional tasks are necessary to determine overall viability of SERAPHIM as a maglev propulsion system. Each of these will be addressed in the CDOT-MTG-CIFGA-SNL Team Project of the Urban Maglev Technology Development Program and are defined in that project's PIP [25].

1. Detailed system analysis to establish specific requirements for not only motor performance such as thrust and power as described in this report, but also requirements related to integration of the motor and its supporting systems such as power supply, cooling, and magnetic shielding in a transit vehicle. The specific geometry selected for the motor will influence the size and weight of these supporting systems. The Preliminary Subsystem Specification, Vehicle Design Requirements, and Final System Performance Specification Tasks of the CDOT project will address these issues.
2. Dynamic testing is needed to evaluate the electrical-to-mechanical energy conversion efficiency of the motor at speeds anticipated for the application. Specifically, it is important this be demonstrated in the appropriate size and speed such that the results are directly scalable to the system anticipated for the transit application. Additionally, dynamic testing is necessary to evaluate the motor control system that will coordinate the proper switching of power to the individual motor coils depending on the position of the track coils for various operation modes such as acceleration, braking, or cruising. Task 16 of the CDOT project is proposed to address these issues by construction of a dynamic test wheel that holds several track coils that are accelerated by a multi-coil SERAPHIM motor. Data from the testbed will provide the dynamic benchmarks for the circuit-based motor design codes and control systems.

SUMMARY

This project has extended the previous studies in many important areas that has resulted in a SERAPHIM motor and power supply capable of propelling a potential urban maglev vehicle over a strenuous route. Using improved analysis tools, the design is self-consistent for thermal, mechanical, and electrical loads, which is a significant improvement over previous concepts. The motor coil and power supply have been fabricated for steady-state endurance testing in a static testbed that includes a cooling system, diagnostics to evaluate mechanical, thermal, and electrical responses, and a support structure. These tests will be conducted in the following phase of this project.

Specifically, this project has accomplished the following results:

1. Conducted analyses with the point-mass, dynamic-response spreadsheet model to establish potential performance for the motor and set requirements for thrust and power. The model was improved to include speed limitations based on route curvature, vehicle tilt, track superelevation, and lateral acceleration limits.
2. Evaluated with this model the thrust and power required to drive vehicles ranging in mass from 23 to 35 tonnes over a potential transit route in the Denver metropolitan area at speeds competitive to the adjacent highway traffic. Information from the Low-Speed Maglev Technology Development Program and the Colorado Department of Transportation I-70 Mountain Programmatic Environmental Impact Study (PEIS) was integrated into the model. We determined that motor power and thrust could be significantly reduced (factor of 3) from estimates made with the previous model due to reduction of vehicle mass and speed limitations required by route curvature.
3. Improved the SERTRAIN lumped-element circuit code to include options for the power supply configuration and operation, and coil geometry definition. The previous concept of using a fixed, 60 Hz frequency power supply was replaced with phase-controlled, variable-frequency inverters to minimize peak reactive power demand. Operation at higher frequency proves better than 60 Hz for efficiency of switching from coil-to-coil, but must be balanced against the increased size of the on-board resonant capacitors and the AC losses in the coil.
4. Developed analytic thermal design models that considered fluid flow and heat transfer in the coil as well as details and design of the components of the external heat rejection system. This tool allowed rapid evaluation of designs and the impact of constraints placed by the mechanical and electrical systems.
5. Developed a mechanical stress analysis model from the CAD drawing models, circuit simulations, magnetic field analysis, and thermal design tools. Complete coil and component models were used to evaluate impact of electromagnetic and thermal-induced loads and set requirements for materials selection.
6. Established the design requirements for powered vehicle coils, track reaction coils or plates, and power and cooling subsystems to achieve the competitive speed along the route by analysis with the electrical, mechanical, and thermal tools described above. This analysis resulted in the rejection of the early baseline coil design concept using radial cooling manifolds for mechanical support and heat transfer due to complexity, and developed a simpler coil designed with axial coolant flow.
7. The use of superconductors for the motor coils was assessed and rejected. This was due to the reduction in efficiency associated with the power to operate refrigeration systems to remove the heat generated by the AC losses in the high-temperature superconductors.
8. Designed a test motor for evaluation under static conditions in a testbed to verify magnetic forces and Ohmic losses. The nominal half-scale motor coil will be capable of steady-state operation at the mechanical, thermal, and electrical stress levels anticipated in the full-scale design. This testbed includes half-scale motor and track coils, inverter power supply, cooling system, diagnostics, and

experiment controls. The testbed structure will allow testing of coils over a range of relative positions that simulate track load conditions.

9. Completed procurement of coils, power supply, and cooling system for the static testbed. Components are being delivered for the assembly and testing phase.
10. The upcoming test phase will be conducted in the next funded project. The depth of design analysis needed during the Initial and Final Design Tasks for the power supply development, improved coil conductor cooling, and minimization of coil losses exceeded cost and schedule estimates in the PIP. This additional effort has resulted in an improved design that will provide an excellent benchmark for our motor design codes and allow accurate assessment of system performance and efficiency.

REFERENCES

1 M. Cowan et al., “The Continuing Challenge of Electromagnetic Launch,” *Megagauss Magnetic Field Generation and Pulsed Power Applications*, M. Cowan and R.B. Spielman, eds., Nova Science Publishers, Inc., New York, 1994, pp.995-1008.

2 B.N. Turman et al., “Co-Axial Geometry Electromagnetic Launch to Space,” Proceedings of AIAA Space Programs and Technology Conference, Huntsville, Alabama, Sept. 27-29, 1994, AIAA 94-4626.

3 B. Marder, “The Physics of SERAPHIM,” Sandia National Laboratories Report, SAND2001-2951, October 2001.

4 B.N. Turman et al., “The Pulsed Linear Induction Motor Concept for High-Speed Trains,” Sandia National Laboratories Report SAND95-1268, June 1995.

5 R.J. Kaye, “Coil Design for SERAPHIM Motor,” Sandia National Laboratories memorandum to Bob N. Turman, September 30, 1999.

6 Project Implementation Plan for FTA project DC-26-7098 “Urban Maglev Transit System Design Using SERAPHIM Propulsion Technology,” January 2001.

7 “Low-Speed Maglev Technology Development Program,” U.S. Dept. of Transportation, Federal Transit Administration report DOT-CA-26-7025-02.1, March, 2002.

8 Colorado Department of Transportation, “I-70 Mountain Corridor Programmatic Environmental Impact Statement,” www.i70mtncorridor.com.

9 W. V. Hassenzahl, "Applications of Superconductivity to Electric Power Systems," *IEEE Power Engineering Review*, May 2000.

10 W. V. Hassenzahl, "More Applications of Superconductivity to Electric Power Systems," *IEEE Power Engineering Review*, June 2000.

11 S. P. Mehta, N. Aversa and M. S. Walker, "Transforming Transformers," *IEEE Spectrum*, July 1997.

12 S. Ige, et. al, "Test Results of a Demonstration HTS Magnet for Minesweeping," presented at 2000 Applied Superconductivity Conference, Virginia Beach, Virginia, September 17-22, 2000.

13 O. O. Ige, et al., "A demonstration HTS magnet for minesweeping," *IEEE Transactions on Applied Superconductivity*, Vol. 10, No. 1, pp. 482-485, 2000

14 FSP 51-41, ASME Transactions, 1929, pp. 287-302.

15 Dykhuizen and Helmich, “User’s manual for IR thermal response code”, June 20, 1994.

16, Industrial Laminating Thermosetting Products, NEMA Standards Publication No. LI1-1998, Specification Sheet-21 NEMA Grade G-10, National Electrical Manufacturers Association, Rosslyn, Virginia, 1998, pp161-168.

17 SolidWorks 2001, three-dimensional solid modeling software, SolidWorks Corporation, Concord, Massachusetts March 2001.

18 Patran, finite element meshing software, release 90, MSC Software Corp., Santa Ana, California, 2001.

19 L.A. Schoof, “EXODUS II: a finite element data model,” Sandia National Laboratories report SAND92-2137, September 1994.

20 M.L. Blanford, “JAS3D, a multi-strategy iterative code for solid mechanics analysis”, Sandia National Laboratories software Release 1.6, March 2001.

21 J.F. Dempsey, “Atheta2exo, a Fortran translator used to couple Atheta_force to Exodus,” Sandia National Laboratories software, March 2001.

22 W.T. Thomson, Theory of Vibration With Applications, Prentice Hall, New York 1972, p.48.

23. Marks’ Standard Handbook for Mechanical Engineers, Eighth edition, T. Baumeister and E.A Avallone, eds., McGraw Hill, New York, 1978, Section 6-63, Table 2.

24 ScotchWeld #1469 epoxy adhesive material specification, 3M Corporation, http://www.3M.com/us/mfg_industrial/adhesives/pdf/SWLPProdSummary.pdf, December 1987.

25 Project Implementation Plan for FTA Urban Maglev Technology Development Program, CDOT-MTG-CIFGA-SNL Team Project, January 21, 2002.